10-25-2017

Constraining Balmer Alpha Fine Structure Excitation Measured in Geocoronal Hydrogen Observations

D. D. Gardner
University of Wisconsin-Madison

E. J. Mierkiewicz
Embry-Riddle Aeronautical University, mierkiee@erau.edu

F. L. Roesler
University of Wisconsin-Madison

S. M. Nossal
University of Wisconsin-Madison

L. M. Haffner
University of Wisconsin-Madison

Scholarly Commons Citation

Gardner, D. D., Mierkiewicz, E. J., Roesler, F. L., Nossal, S. M., & Haffner, L. M. (2017). Constraining Balmer alpha fine structure excitation measured in geocoronal hydrogen observations. Journal of Geophysical Research: Space Physics, 122, 10,727–10,747. https://doi.org/10.1002/2017JA024055

AGU PUBLICATIONS

JGR

Journal of Geophysical Research: Space Physics

RESEARCH ARTICLE
10.1002/2017JA024055

Key Points:
- The Balmer beta/alpha line ratio is explicitly shown to be a function of viewing geometry and solar conditions
- Cascade determined directly from Balmer alpha spectral fits corroborates Balmer beta/alpha line ratio behavior
- The Balmer β/α line ratio constrains forward modeled [H(z)] distributions and Balmer alpha line profile kinematics

Correspondence to:
D. Gardner,
ddgardner@wisc.edu

Citation:
Gardner, D. D., Mierkiewicz, E. J., Roesler, F. L., Nossal, S. M., & Haffner, L. M. (2017). Constraining Balmer alpha fine structure excitation measured in geocoronal hydrogen observations. *Journal of Geophysical Research: Space Physics*, *122*, 10,727–10,747. https://doi.org/10.1002/2017JA024055

Received 19 FEB 2017
Accepted 15 SEP 2017
Accepted article online 19 SEP 2017
Published online 25 OCT 2017

Constraining Balmer Alpha Fine Structure Excitation Measured in Geocoronal Hydrogen Observations

D. D. Gardner[1], E. J. Mierkiewicz[2], F. L. Roesler[1], S. M. Nossal[1], and L. M. Haffner[1]

[1]University of Wisconsin-Madison, Madison, Wisconsin, USA, [2]Embry-Riddle Aeronautical University-Daytona, Daytona Beach, Florida, USA

Abstract Cascade contributions to geocoronal Balmer α airglow line profiles are directly proportional to the Balmer β/α line ratio and can therefore be determined with near simultaneous Balmer β observations. Due to scattering differences for solar Lyman β and Lyman γ (responsible for the terrestrial Balmer α and Balmer β fluorescence, respectively), there is an expected trend for the cascade emission to become a smaller fraction of the Balmer α intensity at larger shadow altitudes. Near-coincident Balmer α and Balmer β data sets, obtained from the Wisconsin H alpha Mapper Fabry-Perot, are used to determine the cascade contribution to the Balmer α line profile and to show, for the first time, the Balmer β/α line ratio, as a function of shadow altitude. We show that this result is in agreement with direct cascade determinations from Balmer α line profile fits obtained independently by high-resolution Fabry-Perot at Pine Bluff, WI. We also demonstrate with radiative transport forward modeling that a solar cycle influence on cascade is expected, and that the Balmer β/α line ratio poses a tight constraint on retrieved aeronomical parameters (such as hydrogen's evaporative escape rate and exobase density).

Plain Language Summary Understanding how hydrogen densities and temperatures change at the top of the atmosphere (near space, actually) is important for climate change and atmospheric evolution investigations. This paper shows how the density distribution of hydrogen at the top of the atmosphere can be inferred using ground-based observations of hydrogen airglow emissions and modeling. The unique variation of these airglow emissions is a useful constraint to help better determine neutral hydrogen temperatures and densities at the top of the atmosphere.

1. Introduction

Ground-based geocoronal hydrogen Balmer α airglow measurements provide a unique opportunity to contribute to three major areas of geocoronal research: geocoronal physics, atmospheric structure and coupling, and exospheric variability. Additionally, an important reason to study planetary exospheres is to learn about the evolutionary loss of species through various escape mechanisms (Hunten & Donahue, 1976). Toward this end, measurements of geocoronal hydrogen, H, enable a better understanding of the physical processes underlying the abundance, transport, and variability of hydrogen through Earth's upper atmosphere (Mierkiewicz et al., 1999). Hydrogen is the dominant and lightest species in the near-collisionless exosphere, and the daughter product of H_2O, H_2, and CH_4 photolysis in the well-mixed mesosphere. Accurately quantifying hydrogen's vertical density distribution profile, [H(z)], photochemically induced vertical transport flux, ϕ, and related exospheric dynamics is a challenging problem critical to not only the study of H aeronomy but also a wide range of atmospheric, near space, and climatological investigations, as well as their associated model validations (Fahr & Shizgal, 1983; Pierrehumbert, 2010). For example, magnetospheric energy dissipation through ring current decay (Daglis et al., 1999), associated plasmaspheric refilling rates (Krall, Huba, et al., 2016; Krall, Emmert, et al., 2016; Krall & Huba, 2016), and the geocoronal response itself to geomagnetic activity (Zoenchen et al., 2017) all depend on the underlying H distribution.

The hydrogen distribution in the upper atmosphere can be constrained by forward model analysis of remote sensing airglow data obtained by rocket, satellite, and/or ground-based observations. Radiative transport code can be coupled to appropriate atmospheric models, and the observed hydrogen airglow phenomena can be replicated by varying the model input parameters (Bishop et al., 2001, 2004). In one such approach, multiple observations along distinct lines of sight, sampling a wide range of viewing geometries, can be used to parameterize forward model retrievals of geocoronal hydrogen parameters (Anderson et al., 1987).

The temporal resolution of these ground-based model/data retrieved aeronomical parameters depends on how quickly the observer can sample a sufficient range of viewing geometries to fully constrain the model. Thus, ground-based observations of the faint hydrogen airglow have typically been obtained by Fabry-Perot interferometers, favored because of their ability to work at relatively high resolving power and high throughput (Roesler, 1974). These instrumental characteristics are needed to accurately separate the airglow emission from the ubiquitous Galactic background while still being able to temporally determine and isolate source intensity variations with viewing geometry (Mierkiewicz et al., 2006).

With regard to geocoronal physics, the interpretation of the Balmer α line profile for kinematic signatures has been limited by uncertainties from excitation mechanisms beyond direct Lyman β excitation such as cascade-induced emission and uncertainties due to residual spectral contamination in the line profile wings from Galactic and terrestrial sources. This, in part, has been due to difficulties in obtaining high spectral resolution Balmer α line profiles with the signal-to-noise ratio (SNR) required to explore perturbations of the Balmer α profile at the 5 to 10% level. Toward this end, Roesler et al. (2014) established that simultaneous observations of geocoronal Balmer α and Balmer β airglow intensities can be used to obtain the cascade contribution to the total Balmer α line profile intensity; that is, the cascade is directly proportional to the Balmer β/α line ratio.

Accounting for the cascade contribution to the geocoronal Balmer α spectral line shape is critical to properly fit and interpret additional excitation mechanisms and exospheric dynamic signatures. For example, a non-thermalized hot hydrogen population in the upper thermosphere, as proposed by Qin and Waldrop (2016), could potentially be evident in sufficiently sensitive, low shadow altitude Balmer α spectra as a broad, symmetric enhancement at the base of the emission line. In a second example, escaping populations of hydrogen in deep shadow altitude observations are predicted to give rise to a faint red shifted spectral signature near the dominant fine structure cascade contribution to the Balmer α line shape (see Chamberlain & Hunten, 1987; Yelle & Roesler, 1985). And while nonauroral collisional excitation components to Balmer α have yet to be identified, photoelectron impact excitation may enhance fine structure components in Balmer α in addition to those from direct solar Lyman series excitation. Note, the expected photoelectron impact excitation contribution to Balmer α is less than a single Rayleigh (Bishop et al., 2001); the Wisconsin H alpha Mapper instrument is sensitive to sub-Rayleigh sources.

Building on the work of Roesler et al. (2014), here we use near-coincident ground-based observations of geocoronal Balmer α and Balmer β line ratios, obtained near solar minimum in 2008 by the Wisconsin H alpha Mapper (WHAM), to corroborate cascade observed directly in high-resolution ground-based Balmer α data sets obtained near solar maximum in 2000 by the Pine Bluff Observatory (PBO) Fabry-Perot interferometer (FPI) (Mierkiewicz, 2002). The WHAM Balmer β/α line ratio variation with viewing geometry also shows, for the first time, that the cascade contribution to Balmer α is explicitly a function of viewing geometry. This relationship not only is useful in constraining cascade contributions to the total Balmer α emission observed in high-resolution line profile observations but is also useful in constraining observations obtained by instruments not fully capable of resolving the cascade themselves (e.g., Gardner et al., 2017). We also show that the unique Balmer β/α line ratio variation with viewing geometry offers a likely forward model constraint toward the retrieval of aeronomical parameters of interest (e.g., [H(z)]).

Because WHAM Balmer β and Balmer α observations share common pointing schemes, astronomical calibration sources, and sample the same atmosphere but are excited by different solar ultraviolet lines (Lyman γ and Lyman β, respectively) with differing transport properties, forward model fitting of the Balmer β/α line *ratio* as a function of viewing geometry provides a tight constraint on the retrieved [H(z)] distribution, largely independent of the absolute instrumental intensity calibration and absolute solar line center flux. Using the nonisothermal radiative transport code developed by the late J. Bishop, *Lyao_rt*, we demonstrate the utility of the forward model approach with illustrative comparisons to both the WHAM and PBO FPI data sets. While a full forward model grid search (see, e.g., Bishop et al., 2004) is beyond the scope of this work, our initial forward modeling of the Balmer β/α line ratio implies that a solar cycle influence on the cascade contribution to the Balmer α emission line may be expected.

2. Background

In this section we review ground-based geocoronal H observational viewing geometry, Balmer α and Balmer β emission, and Balmer α line profile cascade contributions.

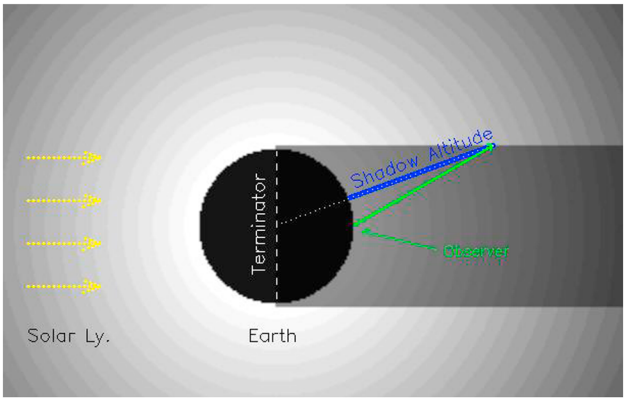

Figure 1. Viewing geometry for an observer at local midnight illustrating shadow distance (the green trace) along the observer's LOS, and the geometrically computed shadow altitude (the blue trace) of the observation. The Sun illuminates from the left; the solar Lyman photons scatter through the geocorona producing the Balmer series fluorescence. Earth's shadow falls to the right. Single and multiple Lyman scattering contribute to the observed Balmer emission along the line of sight, in varying proportions dependent on shadow altitude. (Adapted with permission from Gardner et al., 2017).

2.1. Shadow Altitude Viewing Geometry

Shadow altitude is used to parameterize the base of the observed Balmer series column emission, and the observed variation in this emission is strongest with shadow altitude (as opposed to, e.g., local time). Shadow altitude is defined as the radial distance from the surface of the Earth at which a ground-based observer's line of sight (LOS) intersects the Earth's shadow line. Referring to Figure 1, shadow altitude is the blue chord along the hypotenuse adjoining the vertical dashed terminator line, and the perpendicularly oriented shadow line extending in the antisolar direction.

The altitude of the *shadow line* (i.e., the radius used to define Earth's shadow cylinder) is defined as the altitude at zenith of complete extinction (defined below) at the terminator, for the wavelength of interest. During quiet conditions at sunset, the (vertical) altitude of unit optical depth ($\tau = 1$) for Lyman β occurs at ~135 ± 5 km, primarily due to O_2 photoabsorption with a cross section of 1.63×10^{-18} cm^2; the altitude of complete extinction ($\tau = 100$) we have consistently adopted to geometrically define shadow altitudes for Balmer α fluorescence is 102 km (see, e.g., Bishop et al., 2004). For Balmer β fluorescence, photoabsorption of solar Lyman γ is dominated by N_2 with a cross section of 117.44×10^{-18} cm^2, placing the Lyman γ $\tau = 1$ attenuation altitude at ~268 ± 5 km; the altitude of complete extinction for Lyman γ we have consistently adopted to define shadow altitude is 160 km.

Using a subset of the GLobal airglOW (GLOW) model (Solomon, 2017), we have recently confirmed our adopted altitude of complete extinction ($\tau = 100$) for Lyman β and Lyman γ. The GLOW model routines used here are coupled to NRLMSIS-00 (Picone et al., 2002) with EUVAC (Extreme-Ultraviolet for Aeronomic Calculations) proxy solar irradiances (Richards et al., 1994) and cross sections from Fennelly and Torr (1992) to compute optical depths along zenith as a function of altitude and solar zenith angle (SZA) (see Solomon, 2017, and references therein for more detail). Selected vertical optical depths for various geomagnetic and solar conditions are summarized in Table 1 for an observer at Pine Bluff Observatory, WI (43°N, 270°E), near spring equinox (UTC Day 67), observing toward the zenith at sunset. Under all activity conditions our adopted complete extinction altitudes of 102 km (Lyman β) and 160 km (Lyman γ) appear in order.

Note, integration times for our ground-based Balmer α and Balmer β observations range from 60 s (WHAM intensities) to tens of minutes (coadded high-resolution PBO FPI line profiles). As such, depending on the exact LOS, the shadow altitude during an observation will vary due to Earth's spin by ~10 to 100 km. This spread in the shadow altitude coordinate (used to parameterize the base of the observed column emission) makes the difference of choosing a *shadow line* altitude corresponding to $\tau = 10$ or $\tau = 100$ insignificant for the observations reported here. However, given that we show that the low shadow altitude Balmer β/α line ratio peak may serve as a forward model constraint, this shadow line altitude distinction may be of importance for future Balmer line ratio observations.

2.2. Balmer α and Balmer β Emission

Geocoronal Balmer α (6563 Å) "night glow" is primarily the result of solar Lyman β (1026 Å) scattering by atomic hydrogen in the upper thermosphere and exosphere. This nonconservative scattering results in Balmer

Table 1
Altitudes of Vertical Optical Depths (for SZA = 91)

Solar $F_{10.7}$ (sfu)	Geophysical AP (nT)	Lyman β absorption by O_2 $\tau = 1, 10, 100$	Lyman γ absorption by N_2 $\tau = 1, 10, 100$
220	80	133, 116, 104 km	372, 265, 179 km
220	4	130, 116, 105 km	346, 249, 173 km
70	80	139, 118, 106 km	289, 223, 168 km
70	4	135, 118, 106 km	268, 211, 163 km

Note. Computed using GLOW model. sfu, solar flux unit (1 sfu = 10^{-22} W m^{-2} Hz^{-1}).

Table 2
Balmer α Emission Data Model Components

Component	Transition	λ_{air} (Å)	Δv (km/s)[a]	Relative intensity[b]
1	$3^2D_{3/2} \rightarrow 2^2P_{1/2}$	6562.710	−2.824	0.0016
$2_\odot$	$3^2P_{3/2} \rightarrow 2^2S_{1/2}$	6562.725	−2.133	0.633
3	$3^2S_{1/2} \rightarrow 2^2P_{1/2}$	6562.752	−0.90	0.015
$4_\odot$	$3^2P_{1/2} \rightarrow 2^2S_{1/2}$	6562.772	0.0	0.316
5	$3^2D_{5/2} \rightarrow 2^2P_{3/2}$	6562.852	3.665	0.0029
6	$3^2D_{3/2} \rightarrow 2^2P_{3/2}$	6562.868	4.376	0.0003
7	$3^2S_{1/2} \rightarrow 2^2P_{3/2}$	6562.910	6.299	0.030

Note. Adapted with permission from Mierkiewicz et al. (2006). [a]Component 4 is the reference velocity. [b]Computed for 5% cascade at Balmer α (refer to text).

α fluorescence ~12% of the time. Observed geocoronal Balmer α column emission rates (intensities) depend on the atomic hydrogen density profile, the solar Lyman β line center flux, and viewing geometry. Cascade from hydrogen excitation by higher-order solar Lyman series lines, particularly Lyman γ, also contributes to the observed intensity. Typical zenith observations of geocoronal Balmer α intensities as a function of shadow altitude decrease in an exponential fashion from ~13(±3) to ~2(±1) Rayleighs (R) (±, depending on solar cycle) (Nossal et al., 2001).

While single scattering contributions dominate the observed emission at the lowest shadow altitudes, multiple scattering of Lyman β into the Earth's shadow becomes an increasing fraction of the total Balmer α emission as shadow altitude increases (Anderson et al., 1987; Bishop, 2001; He et al., 1993). The *Lyao_rt* code (described in section 4) indicates that for a ~7 R Balmer α signal observed at a shadow altitude of ~1,000 km, the single to multiple scattered contribution ratio is I_{SS}/I_{MS} ~6; for a ~2 R signal observed at a shadow altitude of ~10,000 km, I_{SS}/I_{MS} ~ 1.5 (Mierkiewicz et al., 1999).

In contrast, the geocorona is optically thinner (by a factor of 0.37) at Lyman γ (973 Å). As such, Balmer β fluorescence (4861 Å; predominantly excited by resonant absorption of solar Lyman γ photons) will have a smaller multiple scattering (and smaller cascade) contribution to its column emission than that of Balmer α. Thus, geocoronal Balmer β intensities are predicted to decrease more rapidly than Balmer α intensities at deeper shadow altitudes; our line ratio observations presented here support this. Typical zenith observations of geocoronal Balmer β intensities are about a tenth of observed Balmer α intensities and have a similar exponential-decreasing variation with shadow altitude.

2.3. Balmer α Cascade

Balmer α emission results from the $n = 3 \rightarrow 2$ transition of atomic hydrogen; the seven fine structure components of this transition are listed in Table 2. In the optically thin approximation, the line multiplet intensity ratios for transitions beginning in the 3S, 3P, and 3D doublet states are, respectively, $I_3 : I_7 = 1 : 2$, $I_2 : I_4 = 2 : 1$, and $I_1 : I_5 : I_6 = 5 : 9 : 1$. As solar Lyman β excitation populates only the 3P levels, this direct resonant fluorescence seen at Balmer α is comprised of only two fine structure transition components, both going from the 3P to the 2S level (components 2 and 4 noted by subscripted solar indices in Table 2).

Excitation by higher-order Lyman series lines, particularly Lyman γ, populate the 3D and 3S (as well as the 3P) levels of Balmer α by cascade. The relative intensities listed in Table 2 are calculated for a 5% cascade contribution (typical of low shadow altitude observations) to the total Balmer α profile. Note, the cascade contributions to the 3P to 2S transitions are 3 orders of magnitude lower than those directly excited by Lyman β resonance fluorescence (Meier, 1995; Nossal et al., 1998) and are not explicitly fit in the cascade model used here.

Roesler et al. (2014) calculated that 90% of cascade excitation by all higher-order Lyman series lines goes into the 3S doublet transition, and therefore, by the multiplet intensity ratio, 60% of the cascade contribution to the net intensity at Balmer α arises from the $3S_{1/2}$ to $2P_{3/2}$ transition alone (component 7). Note, this transition is red shifted by 7.7 km/s from the intensity-weighted centroid wavelength of the Lyman β excited 3P to 2S transitions (components 2 and 4). Thus, effective temperatures obtained from the optimal fit of only a single Gaussian profile to the Balmer α line profile are erroneously high by as much as ~10%, and line center determinations can be in systematic error by several hundred meters per second.

As shown by Roesler et al. (2014), Balmer β intensity observations provide a direct measure of the total excitation by solar Lyman γ and therefore a direct estimation of the dominant cascade contribution at Balmer α. Because cascade is proportional to the Balmer β/α line ratio, and Balmer β fluorescence decreases more rapidly than Balmer α with shadow altitude, the cascade contribution to Balmer α can also be expected to fall off with increasing shadow altitude; our results show this for the first time. Cascade contributions based on Balmer β estimates of Lyman γ excitation can also be compared with measurements of the cascade emission from Balmer α line profile observations in which the cascade component is explicitly fit. Ultimately this method may aid in the identification of other excitation mechanisms (e.g., photoelectron impact), or population redistribution contributions (e.g., hot or escaping components), through the presence of line profile red wing components in excess of the cascade contribution predicted by Balmer β and measured in Balmer α.

Collisional excitation signatures from photoelectron impact or symmetric charge exchange in the Balmer α line profiles could be detected as enhancements to the solar excited fine structure cascade components 1, 5, 6, and 7 (i.e., predominantly in the "red wing"). These mechanisms excite all fine structure components in intensity ratios distinct from solar Lyman β and Lyman γ excitation. However, the signatures of photoelectron impact and symmetric charge exchange, both essentially two-body reactions that go like the square of the local density, will exhibit a much more rapid *decrease* as a function of observed shadow altitude (as opposed to the solar Lyman γ induced cascade variation with shadow altitude) (Bishop et al., 2001, Mierkiewicz et al., 1999, 2006; Roesler et al., 2014; Bishop et al., 2001).

The kinematic signature of escape in ground-based observations is expected to exhibit a slow spectral red wing *increase* as a function of observed shadow altitude, as well as a net blueward depletion biasing the overall line profile, both due to H population redistribution (i.e., satellite → escape) arising from radiation pressure dynamics and plasmasphere interaction (Bishop & Chamberlain, 1987). The blueward biasing was first observationally suggested by Meriwether et al. (1980) with deep shadow altitude Fabry-Perot observations made from Arecibo Observatory (Puerto Rico). To definitively distinguish the escape population component in ground-based line profile observations, that is, to show a shadow altitude dependent residual correlation between both blueward profile biasing and red wing enhancement, great care with line center determination, Galactic background correction, solar excited cascade, and multiple scattering component corrections would be needed.

Previous 2000–2001 PBO observational results, from fitting high-resolution (R = 80,000) FPI geocoronal Balmer α emission data sets with a full fine structure cascade model suggested an empirical cascade contribution of 5% ($\pm$3%) (Mierkiewicz et al., 2012); however, no clear cascade trend with shadow altitude was identified. Here we show that reexamination of a subset of this Balmer α spectral data, by careful coaddition of spectra binned by shadow altitude, suggests a cascade trend as predicted by Roesler et al. (2014). Further, our results show the cascade trend identified in the high-resolution Balmer α spectra corroborates the lower resolution WHAM geocoronal line ratio trend, and that a solar cycle influenced variation between them is supported by modeling.

3. Observations

In this section we describe the WHAM and PBO FPI instruments, their nebular calibration, and Balmer α and Balmer β data selection criteria. We discuss the fits to the spectral data sets obtained by each instrument, our empirically derived method for fitting the WHAM observed intensity *variations* with shadow altitude, and the determination of cascade emission from both WHAM and PBO data.

3.1. FPI Characteristics, Calibration, and Data Selection

We have obtained unprecedented sets of near-coincident measurements of extremely faint geocoronal Balmer α and Balmer β line intensities with WHAM, a highly sensitive Fabry-Perot interferometer (FPI) developed at the University of Wisconsin (Haffner et al., 2003; Tufte, 1997). WHAM covers a 200 km/s (4.4 Å at Balmer α) spectral region with 12 km/s spectral resolution ($R \approx$ 25,000) from a 1° field of view (FOV) on the sky (Tufte, 1997). WHAM data sets from 2008 used here were obtained during WHAM's operation at Kitt Peak National Observatory (KPNO), AZ (31.98°N, 248.40°E) from 1997 to 2008. WHAM can detect a 0.15 R signal (at 3σ certainty) within 30 seconds. This sensitivity makes WHAM an exceptional instrument for geocoronal Balmer α and Balmer β *intensity* observations – however, WHAM does not have sufficient resolving power to adequately characterize cascade perturbations in the Balmer α line profile wings (or determine the Balmer α line profile's Doppler width variations, $<\sim$7 km/s).

WHAM Balmer α and Balmer β absolute intensity calibrations are tied to astronomical nebular emission sources, specifically the North American Nebula (NAN; NGC 7000) and the large HII region surrounding the B1 III star Spica (α Vir), (Haffner et al., 2003; Madsen & Reynolds, 2005; Scherb, 1981). NAN's surface brightness (toward Galactic longitude, l = 85.6°, and latitude, $b = -0.72°$) within WHAM's 1° FOV was calibrated to 800 R (±10%) at Balmer α, and 157 R (±10%) at Balmer β. For Balmer α, WHAM's canonical conversion is 1 R (km $s^{-1})^{-1}$ = 22.8 ADU/s (i.e., the count rate of the charge-coupled device (CCD)'s analog to digital units). Accounting for relative filter transmission, CCD, and optics response ratios for Balmer β relative to Balmer α, the canonical conversion for Balmer β is 1 R (km $s^{-1})^{-1}$ = 40.4 ADU/s (refer to Madsen & Reynolds, 2005, for more details). The uncertainty in absolute intensities due to nebular calibration, for both WHAM and the PBO FPI instruments, is ∼10%. Tropospheric scattering also constitutes a possible enhancement to ground-based observations (Leinert et al., 1998; Hong et al., 1998). The net possible intensity enhancement due to tropospheric scattering here is expected to be less than 15% (Bishop et al., 2004; Nossal et al., 2008; Shih et al., 1985).

The high-resolution FPI observations of Balmer α used here to directly determine the cascade line profile contributions were taken between 2000 and 2001 at Pine Bluff Observatory, WI (PBO; 43° N, 270° E). These PBO data sets, and the high-resolution FPI instrument used to acquire them, were detailed in Mierkiewicz et al. (2006). The PBO FPI covers a 75 km/s (1.65 Å at Balmer α) spectral region with 3.75 km/s spectral resolution (R = 80,000) from a 1.4° FOV on the sky. Comparative geocoronal and NAN observations, at varying FOV's and zenith distances, yielded 1 R (km $s^{-1})^{-1}$ = 3.48×10^{-2} ADU/s (raw "Analog-to-Digital Units" per second), giving NAN an estimated 650 R ±10% within the 1.4° beam centered at $l = 85.6°$, $b = -0.72°$ (refer to Mierkiewicz et al., 2006).

All WHAM geocoronal observations shown here have been restricted to zenith angles less than 45°. Observations were obtained away from the plane of the Galaxy ($|b| > 15°$) at Doppler shifts greater than 10 km/s from Galactic emission (VLSR > 10 km/s). Solar and lunar depression angles of the observations were >95° (i.e., "clear moonless nights") to avoid being contaminated by sky background or scattered sunlight. All PBO FPI Balmer α spectra were similarly restricted, but more stringently away from the plane of the Galaxy ($|b| > 60°$). Both WHAM and PBO FPI observations were taken at fixed right ascension and declination.

3.2. FPI Spectral Line Profile Reductions

Both WHAM and the PBO FPI employ the technique of annular summing spectroscopy. Details of this technique and its advantages for aeronomy studies are described in Coakley et al. (1996). Spectra are fit using the command line-driven, Fudgit-based spectral fitting macropackage developed by R.C. Woodward. The "VoigtFit" (VF) program uses least squares chi-minimization analysis to fit multiple Voigt profiles to one dimensional data, and allows instrumental profiles to be convolved in the fits. Voigt line parameters (width, center, and area) can be constrained by (and linked to) other Voigt lines, for example, the fine structure wavelengths' *relative* spectral spacing can be held constant, but the overall line centroid location can be a free fitting parameter, and similarly with the Doppler width.

To fit the PBO FPI Balmer α spectra, we use a sum of Gaussian functions to account for the dominant asymmetry resulting from fine structure cascade excitation. As shown in Table 2, using Meier (1995) atomic parameters, we link the hydrogen fine structure components in two clusters—the first cluster links the two solar Lyman β excited components (the 3P → 2S transition), constrained in a 2:1 *relative* area ratio per the multiplet rules, and the second cluster similarly links the remaining five cascade components' relative areas. In this process, the wavelength-integrated intensities of the two clusters are free fitting parameters, thus allowing determination of the relative cascade contribution to the line profile.

Prior to fitting, PBO spectra were coadded by shadow altitude bin to boost the signal to noise of the line from which to determine cascade. Shadow altitude bins for each night of observations were set by the requirement to have less than six observations per bin—more than six resulted in a subdivision of the bin. Shadow altitude bin sizes ranged from <500 km at low shadow altitudes, where intensities vary with shadow altitude most rapidly, to no more than ∼1,500–2,000 km at the deeper shadow altitudes, where intensities become relatively constant. Each PBO FPI Balmer α spectra had been previously fit using a full cascade model (Mierkiewicz et al., 2006), and the original fit centroid parameters were used to shift and register the bin-selected spectra to a common spectral baseline before coaddition. The resulting improvement in determined cascade was modest, with errors on the order of ∼1–3%. However, a shadow altitude trend is now notable in these weighted additions (refer to section 3.4).

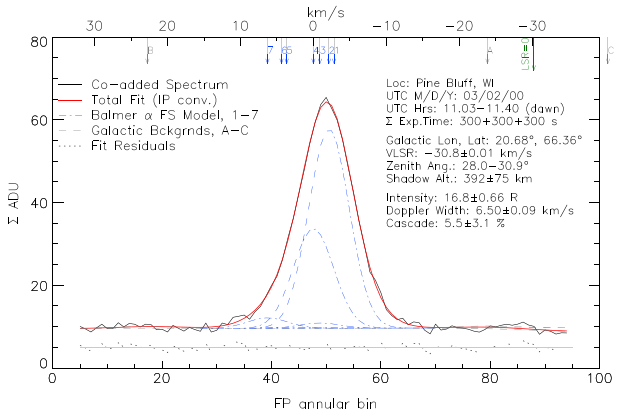

Figure 2. PBO FPI coadded (x3) geocoronal Balmer α spectrum (black), and the seven fine structure components (blue, dashed) comprising the total cascade model fit (red). Two atmospheric (*A* and *B*) and one Galactic background (*C*) component were also accounted for in the fits; residuals are plotted beneath. Components from Table 2 are listed along the top abscissa, where the kilometers per second scale is relative to component 4. These coadded spectra were obtained on 2 March 2000 at Pine Bluff Observatory, WI, near solar maximum over several tens of minutes toward a constant-viewed low-emission Galactic region, just before sunrise. The shadow altitude (and zenith angle) at the beginning of the first coadded observation was 467 km (28°), and by end of the last observation, it was 317 km (30.9°).

The WHAM Northern Sky Survey allows Galactic emission components to be fixed during the fitting of each coadded PBO FPI spectrum. In order to match FOV differences between the WHAM and the PBO FPIs, a flux-weighted approach was used to account for the Galactic components (Gardner et al., 2017). Although the Doppler width and spectral position of the Galactic emission was fixed, the total Galactic emission intensity was a free parameter in order to account for differences in instrumental absolute response. However, similar to the cascade fitting model, the intensity *ratio* of the Galactic components present in the background was constrained to that reported by WHAM. In addition, two faint interloping atmospheric emission lines reported by Hausen et al. (2002) were also similarly corrected for in the coadded PBO FPI data sets. Finally, rather than deconvolve spectra from the instrumental profile, thorium emission line instrumental profiles were convolved in the fits, as described by Mierkiewicz et al. (2006), to accurately constrain Galactic emission component widths and retrieve geocoronal emission fine structure components.

Figure 2 shows an example PBO FPI coadded spectrum of three, 5 min, high-resolution Balmer α observations made near dawn, within ~20 min of each other, and all toward a Galactic "off" region of extremely low Galactic emission (~0.56 R). The net signal (black trace) and the resulting fit (red trace) are overplotted on top of the fine structure components (blue dashed traces). Noting the top abscissa, the spectrum goes from red to blue. All fine structure component locations are indicated by number, following Table 2; the spectral scale in kilometers per second is referenced to component 4. The background components A and B are the locations of atmospheric interloping emission lines, of negligible intensity here, but fit and accounted for nonetheless. Background component C is for a WHAM-observed Galactic emission component well away (blueward) of the geocoronal emission line center. Note, the bulk of the fit recovered cascade contribution of ~5.5% to the total geocoronal Balmer α intensity (16.8 R) predominantly arises in the spectral red wing, from fine structure component 7.

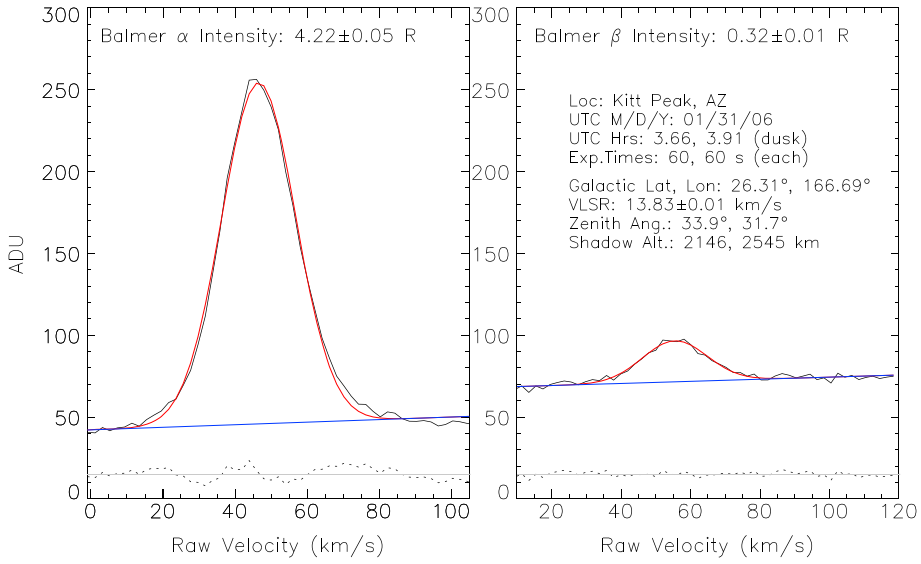

Figure 3. A near-coincident pair of observations made by WHAM toward a well-characterized low Galactic emission "off" region. (left) Balmer α and (right) Balmer β exposures were both 60 s, obtained a few hours after dusk at Kitt Peak, AZ, near solar minimum on 31 January 2006. The Balmer α spectrum was taken at a 33.9° zenith distance and 2,146 km shadow altitude; 15 min later, the Balmer β spectrum was obtained at 31.7° zenith distance and 2,545 km shadow altitude. A single Gaussian fit (red) with a slope (blue) was found to be sufficient to retrieve the intensities from the (black) data; residuals are plotted below.

WHAM Balmer α and Balmer β spectra were fit with a single Gaussian function on a slightly sloping background. All WHAM intensities were corrected for atmospheric extinction using average transmission factors for KPNO, $T_{H\alpha} = 0.93$ and $T_{H\beta} = 0.847$ (Haffner et al., 2003). Due to WHAM's inability to resolve Balmer line profiles, the WHAM spectra were not corrected for instrumental broadening. Figure 3 is an example of near-coincident Balmer α (left) and Balmer β (right) spectra obtained with WHAM. Each exposure was 60 seconds toward a Galactic "off" region a few hours after local dusk. The geocoronal Balmer β intensity (0.32 R) is ~0.1 that of Balmer α (4.22 R). Observations were 15 min apart, leading to a shadow altitude difference of 400 km between them. The near-coincident 60 s WHAM observations used here were carried out in "block" mode, where Balmer α was observed for 10–15 min, and then immediately after Balmer β was observed for 10–15 min, each set toward the same low Galactic emission look direction. To obtain the Balmer line ratio, the intensity variations for each emission with respect to shadow altitude must be fit (and then numerically divided) since the observations are not exactly coincident in shadow altitude (or time). To obtain sufficient shadow altitude coverage for this study, several dates of WHAM data were used.

3.3. Fitting of Intensity Variations With Shadow Altitude

In general, our Balmer intensities are observed to be smoothly varying. There are three simple physical features (conditions) that an empirically derived intensity fitting function ansatz should capture: (1) the intensity increases significantly and very rapidly toward low shadow altitudes approaching the dawn and dusk terminator, (2) the smooth and flat central minimum intensities at higher shadow altitudes looking down Earth's shadow (i.e., adjoining the local dawnside AM and duskside PM intensity variations), and (3) the asymmetry of average dawn intensities being ~10–20% higher than their dusk counterparts (Bailey & Gruntman, 2011; Kerr et al., 2001; Mierkiewicz et al., 2012; Tinsley, 1968).

One empirically motivated function that captures all three of these intensity conditions is a composite hyperbolic tangent function. The form $A\tanh[B(C + ix)]$ provides rational periodicity needed by conditions 1 and 2 to simultaneously fit AM and PM intensity variations spanning any "midnight" shadow altitude coordinate. Adding a 2° polynomial gives the asymmetry needed by condition 3. To fit in x then, intensity data are "unfolded," going from dusk to dawn (that is, $-14{,}000 < x < 14{,}000$ km here), about a midnight ($x = 0$) shadow altitude coordinate (14,000 km). This range was set approximately twice as deep as the deepest shadow altitude observed here to assure a slope of zero is fit at $x = 0$. Our asymmetric hyperbolic tangent fitting function then, is

$$y = A\tanh[B(C + ix)] + D + Ex + Fx^2 \tag{1}$$

where A, B, C, D, E, and F are fit parameters for the intensity, y, as a function of shadow altitude, x. The real part of the solution will give a nearly flat intensity slope at the midnight shadow altitude coordinate. In the fitting process of equation (1), fit parameter D was held fixed so that the recovered minimum, at the deepest shadow altitude, smoothly reproduces the observed minimum (shared by both dawn and dusk side); ~1–2 (~0.1) R for Balmer α (Balmer β). Due to the scatter in our present data set, we found it advantageous to fit equation (1) to the log(intensity) variations.

We also fit the AM and PM intensity variations independently, using a sum of exponentials motivated by the physical process of multiple scattering through the exosphere. The first exponential shown in equation (2) could represent the single scattering component's variation with shadow altitude, while the second exponential could represent the multiple scattering component:

$$y = Ae^{Bx} + Ce^{Dx} + E \tag{2}$$

where exponent fit parameters B and D should converge to be negative (and A and C positive). However, to provide physically meaningful solutions regarding the nature of scattering variations when fit to the intensity data, the amplitudes and exponents must be constrained with further underlying mechanistic information. Fit parameter E, however, provides a directly meaningful physical quantity—the expected intensity minimum at a deep shadow altitude.

Overplotted on the log intensity scale in Figure 4 is the (dark gray) fit of equation (1) to the log(intensity) variation, and the (blue) fit of equation (2) to the intensity variation, for both Balmer α (top) and Balmer β (bottom) WHAM data sets (light gray symbols). The fits were performed using a Levenberg-Marquardt least squares minimization algorithm in IDL, v8.2 ("LMfit.pro"). Cascade, listed above the abscissa in Figure 4, is computed by method of Roesler et al. (2014) at representative shadow altitudes using the intensity fits

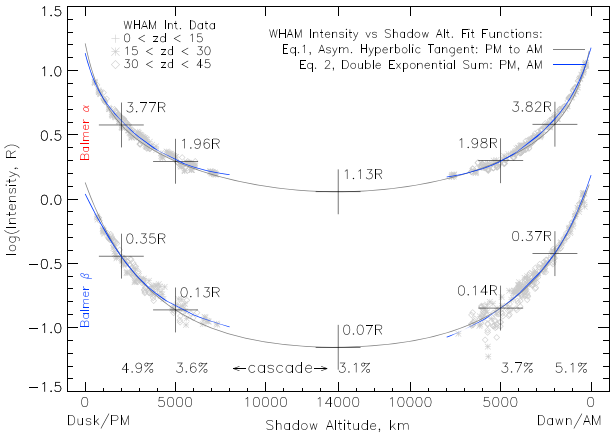

Figure 4. WHAM-observed Balmer α (top) and Balmer β (bottom) log(intensity R) variations verses shadow altitude (km), collected from five nights at Kitt Peak, AZ. The abscissa coordinates are for observational shadow altitudes unfolded about midnight (14,000 km), and relative to the dusk/PM or dawn/AM horizon (refer to text). For a particular shadow altitude, the Balmer β intensity is ~0.1 as bright as Balmer α. Over plotted traces show the fits of equations (1) (dark gray) and (2) (blue) to the Balmer intensities; these functions were used to determine the cascade variations (by division) shown in Figure 5. Sample % cascade values printed above the axis are computed from the Balmer intensities marked by large black crosses at shadow altitudes |2,000|, |5,000|, and |14,000| km.

at these altitudes (at the black crosses in Figure 4). For example, at a 2,000 km shadow altitude after sunset there is an expected cascade contribution to the Balmer α line profile intensity of $0.52 \times I_\beta / I_\alpha \times 100\% = 4.9\%$. The recovered fit parameters (and errors) for equations (1) and (2) are listed in Table 3.

When equation (2) was fit to the Blamer α intensity (R) data, fit parameter *E* was allowed to be free for both the AM/dawn and PM/duskside fits. Both AM and PM fits agree that the Balmer α intensity minimum at a deep shadow altitude is ~1.38 R. This is in agreement with the minimum intensity value found (1.13 R) when equation (1) is *simultaneously* fit to the Balmer α AM and PM log(intensity, R) data. Note, parameter *D* is held fixed for convergence of equation (1), but *D* itself does not represent the minimum.

To obtain convergence with equation (2) when fitting the noisier Balmer β intensity data, fit parameter *E* was eventually fixed to the minimum intensity value found (~0.065 R) in the fitting of equation (1) to the Balmer β log(intensity) data spanning PM to AM. Given these fit parameter sensitivities to the scatter in the data, we found it advantageous to fit both intensity and log(intensity) variations with equations (1) and (2); when one equation fails to give acceptable fit convergence, the other can be used to constrain it.

3.4. Cascade Variation With Shadow Altitude

As shown by Roesler et al. (2014), the cascade contribution to the Balmer α line profile can be obtained by taking the ratio of near-coincident observations of Balmer β and Balmer α intensities. Using the fits to the WHAM observations described by equations (1) and (2) (and shown in Figure 4), the line ratio variation as a function of shadow altitude can then be determined. This result can be compared to the cascade obtained *directly* by fitting of the high-resolution Balmer α line profile (i.e., from the fine structure cascade model spectral fit shown in Figure 2).

As an example of this, the cascade variation with shadow altitude obtained by taking the numeric ratio of the fit of equations (1) (the dark gray curve) and (2) (the blue curve) to Balmer β and Balmer α intensity

Table 3
WHAM Intensity Variation Fit Coefficients for Equations (1) and (2)

	Log(intensity) Equation (1)	Intensity Equation (2) PM	Intensity Equation (2) AM
		Balmer α Fit Parameter	
A (Δ*A*)	2.95E+04 (8.1E+09)	5.24E+00 (1.3E+00)	6.15E+00 (3.3E−01)
B (Δ*B*)	9.61E−05 (1.3E−06)	−2.62E−03 (7.5E−04)	−2.16E−03 (2.1E−04)
C (Δ*C*)	1.29E−02 (3.5E+03)	7.03E+00 (4.7E−01)	7.60E+00 (4.1E−01)
D (Δ*D*)	2.00E−02 (fixed)	−4.92E−04 (3.6E−05)	−4.99E−04 (2.7E−05)
E (Δ*E*)	2.41E−07 (1.0E−07)	1.41E+00 (7.0E−02)	1.34E+00 (5.5E−02)
F (Δ*F*)	2.33E−09 (1.8E−10)	NA	NA
		Balmer β Fit Parameter	
A (Δ*A*)	3.98E+04 (1.8E+09)	1.94E−01 (1.2E−01)	6.02E−01 (8.3E−02)
B (Δ*B*)	6.64E−05 (4.4E−07)	−1.98E−04 (9.6E−05)	−4.02E−04 (3.1E−05)
C (Δ*C*)	3.18E−01 (1.4E+04)	8.41E−01 (9.1E−02)	8.72E−01 (6.3E−02)
D (Δ*D*)	2.00E−03 (fixed)	−8.13E−04 (1.2E−04)	−1.41E−03 (1.6E−04)
E (Δ*E*)	8.13E−07 (2.3E−07)	6.00E−02 (fixed)	6.00E−02 (fixed)
F (Δ*F*)	−1.16E−09 (3.8E−10)	NA	NA

Note. NA, not applicable.

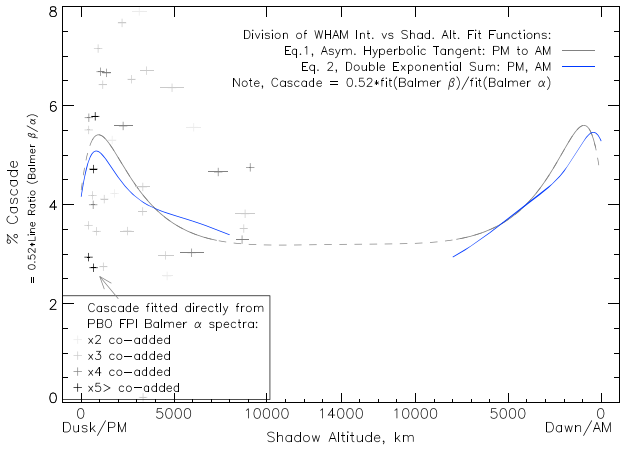

Figure 5. Balmer β/α line ratio (or, equivalently, Balmer α expected cascade) variation verses shadow altitude, as obtained by division of the fits of equations (1) (dark gray) and (2) (blue) to the observed intensity variations in Figure 4 (WHAM, near solar minimum). The shallow shadow altitude line ratio peak offers a new forward modeling constraint. The middle dashed (dark gray) line is a reminder of the fit extrapolation in lieu of intensity data at these altitudes. The crosses on the duskside (color range indicating SNR increase by coaddition) are Balmer α cascade values determined directly from fine structure cascade model fits (e.g., Figure 2) to the high-resolution coadded spectra (PBO, near solar maximum). Horizontal cross lengths represent the average shadow altitude bin size for spectra coaddition; vertical errors, ±3%, are omitted for clarity.

variations obtained by WHAM is plotted in Figure 5. A consequence of the multiple scattering differences between Lyman γ and Lyman β is immediately visible in the curves as a low shadow altitude peak at both dawn and dusk. The derivative of this peak with respect to shadow altitude is a potential forward model constraint (refer to section 5.1). Note, the magnitude and peak location difference between dawn and dusk reflects the underlying AM and PM asymmetry in intensities, and presumably H densities. The overplotted crosses in Figure 5 are cascade measurements obtained directly from high-resolution line profile fits to the PBO FPI spectra (not separated by AM and PM observations—in order to better compare agreement of the sharp rise in cascade seen in both PBO FPI and WHAM data at low shadow altitude).

The direct cascade measurements (crosses) in Figure 5 trace a similar behavior predicted by the line ratio determined cascade; both rise steeply and peak at low shadow altitudes and then more gently decrease toward midnight. The direct cascade measurements' descending slope (crosses) also appears, on average, to be a few percent higher than the similarly descending line ratio determined cascade. However, recall that the direct PBO FPI coadded Balmer α cascade data are for solar maximum, while the WHAM line ratio cascade results is for solar minimum; thus, a quantitatively direct comparison should be interpreted with caution. This will be discussed further in section 4, in the context of forward modeling.

WHAM's absolute calibration uncertainty (±10%, for both Balmer α and Balmer β intensities) is tied to the uncertainty in the NAN nebular calibration source. To assess the magnitude of this calibration uncertainty inherent in our WHAM-derived Balmer β/α line ratios variation, we scaled the Balmer intensity data points (Figure 4) by ±10%, refit each with equations (1) and (2), and then took the ratio of all permutations to generate displaced line ratio (or equivalently, cascade) curves; refer to Figure 6. The connecting dashed lines denote fit extrapolation beyond where there are available intensity data.

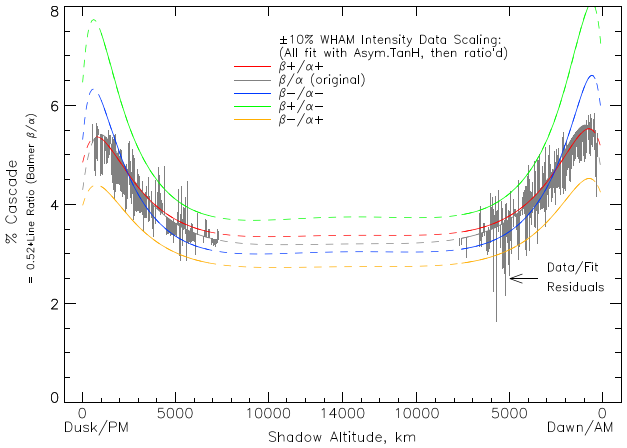

Figure 6. All permutations of Balmer β/α line ratios (cascade), after scaling the WHAM intensity data by ±10%, to simulate the range of derived uncertainty resulting from calibration error. The *largest* overall differences in cascade are seen when Balmer α and Balmer β intensity variations are oppositely scaled, as expected for a function that depends on a *ratio*. equation (1) was exclusively used to refit the scaled Balmer β and Balmer α intensity variations with shadow altitude. Note, the original dark gray curve here is the same as that plotted in Figure 5, and the fit residual marks traced off it (refer to text) indicate the propagated noise from the intensity variation fits using equation (1).

Also plotted in Figure 6 are dark gray fit residual marks, traced away from the original dark gray cascade curve. The magnitude of the residuals at each shadow altitude coordinate was obtained by dividing each individual Balmer α (Balmer β) intensity data *point* into the fitted *curve* for Balmer β (Balmer α) intensity variation. Fit residuals represent the propagated noise in the cascade curve due to imperfect fits of the Balmer intensity variations and (closely) translate with the aforementioned scalings. Notice that the magnitude of fit residuals rarely exceeds the bounds of uncertainty due to calibration error, the upper (green) and lower (orange) curves in Figure 6. The fit residuals are also rather evenly distributed upward and downward across shadow altitude on the dark gray cascade curve. While our exploratory results here preclude robust statistical analysis, this strongly indicates that (1) despite a 10% calibration uncertainty in WHAM-observed Balmer intensities, the error in cascade variation with shadow altitude is within ~1% (by eye, here), and (2) the fit of equation (1) appears to be sufficiently capturing the average intensity variation characteristics with shadow altitude.

4. *Lyao_rt* Forward Modeling

Lyao_rt is an atomic resonance radiative transport code for computing hydrogen (and helium) Lyman series volume excitation rates (source functions) and line-of-sight radiances through a background model atmosphere. Using the complete frequency redistribution approximation of Anderson and Hord (1977) to solve the transport equation in integral form,

Table 4
Daily Averaged Solar and Geophysical Conditions

Year	UTC DOY	*Dst* (nT)	AP (nT)	$F_{10.7}$ (sfu)	Lyman$_{\odot}$ α (10^{11} ph cm^{-2} s^{-1})
		WHAM Observation Dates Near Solar Minimum			
2006	31	−0	1	75.8	3.79
2008	41	−4	11	70.5	3.55
2008	45	−18	10	68.8	3.53
2008	67	−16	3	69.4	3.56
2008	71	−23	17	69.3	3.51
Average	50	–	8.4	70.7	Ly$^{a}_{\odot}$ β/γ = 54.69/10.28
		PBO FPI Observations Dates Near Solar Maximum			
2000	59	−18	16	218.1	5.32
2000	62	−28	18	217.6	5.53
2000	63	−8	4	204.2	5.53
2000	64	−3	4	198.4	5.53
2000	65	2	4	208.6	5.54
2000	66	−5	10	218.1	5.53
2000	67	−23	15	218.8	5.50
2000	270	−42	27	225.6	5.48
2000	271	−33	15	213.5	5.61
2000	272	−24	12	204.0	5.66
2000	273	−22	7	196.9	5.63
2000	277	−47	30	196.6	5.68
2000	327	−17	9	186.3	5.72
2000	329	−2	6	195.4	5.80
2000	338	−10	7	160.3	6.09
2001	48	−3	3	126.7	4.81
2001	49	−3	3	128.1	4.83
2001	52	−4	6	141.2	4.94
Average	50	–	10.8	189.5	Ly$^{a}_{\odot}$ β/γ = 82.68/15.54

Note. All values retrieved from https://omniweb.gsfc.nasa.gov. [a](10^{8} ph cm^{-2} s^{-1} Å^{-1}). DOY, day of year.

Lyao_rt-computed radiances account for nonisothermal density distributions in a spherical geometric framework. Although *Lyao_rt* explicitly accounts for multiple scattering and nonisothermal conditions, indirect cascade and collisional excitation complications are not accounted for (i.e., only the direct, Lyman-excited Balmer fluorescence branching ratios are used). The spherically symmetric RT code boundaries extend from the lower thermosphere out to ~20 R_e. Lyman absorption in the lower thermosphere is computed assuming constant absorption cross sections for the respective species (refer to Bishop, 1999, for further details).

Background thermospheric temperature and density profiles of the major thermospheric species (O, O_2, and N_2) are obtained here from NRLMSIS-00 (Hedin, 1991; Picone et al., 2002). [H(z)] profiles from NRLMSIS-00 can also be used (essentially assumed to be in diffusive equilibrium above ~200 km), but the resulting thermospheric H column abundances have consistently been too small for *Lyao_rt* intensity profiles to match Balmer α data (Bishop et al., 2001). Alternatively, *Lyao_rt* can be independently supplied with three thermospheric H parameters (the mesospheric peak density, $[H]_{peak}$, exobase density $[H]_{exo}$, and H flux, ϕ) to parameterize [H(z)] by modifying NRLMSIS-00 and self-consistently computing the diffusive flow of hydrogen to the exobase (still using the NRLMSIS-00 thermospheric temperature profile) (refer to Bishop, 2001, for more details).

Extension of hydrogen into the exosphere is based on the Bishop (1991) analytic exosphere model. Evaporative satellite population parameters can be used, where both the satellite and ballistic population's kinetic distribution functions (KDF) are set by the NRLMSIS-00 exobase temperature, T_c, and density, n_c.

Table 5
Lyao_rt and NRLMSIS-00 Model Parameters

	Solar maximum		Solar minimum	
	PM	AM	PM	AM
		MSIS00/evap		
T_c	1233	970	788	654
n_c	3.9×10^4	6.0×10^4	1.7×10^5	3.9×10^5
		H-param/evap		
T_c	1233	970	788	654
$[H]_{exo}$	3.0×10^4	3.4×10^4	1.6×10^5	2.0×10^5
ϕ	8.0×10^7	8.0×10^7	7.0×10^8	7.0×10^8
$[H]_{peak}$	1.5×10^8	1.5×10^8	1.5×10^8	1.5×10^8
		H-param/T-sat		
T_c	1233	970	788	654
$[H]_{exo}$	3.0×10^4	3.4×10^4	1.6×10^5	2.0×10^5
ϕ	8.0×10^7	8.0×10^7	7.0×10^8	7.0×10^8
$[H]_{peak}$	1.5×10^8	1.5×10^8	1.5×10^8	1.5×10^8
T_s	900	700	600	575
n_s	2.2×10^5	2.2×10^5	7.0×10^6	7.0×10^6

Note. Units: T (K), n and [H] (cm^{-3}), and ϕ ($cm^{-2}\ s^{-1}$).

Alternatively, to simulate the population redistribution effects of plasmaspheric charge exchange due to exobase $T_{ions} > T_{neutrals}$, the satellite population's KDF can be independently set with its own temperature and density (T_s and n_s). In all cases, ignoring thermospheric dynamics, a spherically uniform exobase temperature and density are used to generate the exospheric populations (Bishop, 1999).

Our exploratory modeling uses *Lyao_rt* parameters adopted from other geocoronal forward modeling studies (Waldrop & Paxton, 2013; Bishop, 1991; Bishop et al., 2001, 2004), to assess the observed Balmer line ratio variation with shadow altitude. Bishop et al. (2001, 2004), Nossal et al. (2012), and recent analysis of the Thermosphere Ionosphere Mesosphere Energetics and Dynamics satellite's Global Ultraviolet Imager (GUVI) Lyman α limb scan data by Waldrop and Paxton (2013) all show that using *Lyao_rt* evaporative exosphere conditions alone give forward model solutions that cannot be fully reconciled with observational data. In all cases, independent specification of satellite population parameters was needed to best match the airglow data. Further, in the case of the GUVI Lyman α data, even independent satellite parameter specifications were deemed insufficient to adequately forward model the limb scan observations, and this led directly to the *Lyao_rt* code modification described by Qin and Waldrop (2016) and their postulation of an upper thermospheric population of hot hydrogen.

Lyao_rt LOS radiances here were computed for an observer at KPNO (where WHAM observations were made), observing toward zenith across the range of shadow altitudes sampled by our intensity data, on a UTC day 50. To compute hydrogen distributions for *Lyao_rt*'s exospheric extension and radiative transport integration, the NRLMSIS-00 base thermosphere was parameterized by our observations' seasonal average AP and $F_{10.7}$ values for solar maximum and minimum conditions, calculated at 7 p.m. and 5 a.m. local time. Table 4 lists observation dates, daily average AP and $F_{10.7}$ values, and the solar Lyman α solar index and *Dst* (discussed in section 5.3.1). Since our observational results are effectively averaged by combining data from all dates during each solar period to build sufficient shadow altitude coverage, average solar and geophysical conditions were used to parameterize NRLMSIS-00 (see Table 4). Input average AP, $F_{10.7}$, and solar line center fluxes are held fixed for all model runs.

As precedented in Bishop (1999), solar Lyman β line center fluxes input for *Lyao_rt* code were estimated using (1) the daily Lyman α solar index, followed by (2) the assumption that solar Lyman α line center fluxes are *numerically* roughly equal to line-integrated fluxes, and (3) the line center estimate that $Ly_\odot\beta = (1/66) \times Ly_\odot\alpha$; refer to Table 4. Our *Lyao_rt* computed input solar maximum and minimum Lyman β line center fluxes, $\sim 8.3 \times 10^9$ and $\sim 5.5 \times 10^9$ ph $cm^{-2}\ s^{-1}\ Å^{-1}$, are in agreement with solar cycle values previously reported by Anderson et al. (1987) and Warren et al. (1998). The solar Lyman β line center flux varies *on average* by *approximately* a factor of 2 over the solar cycle. Solar Lyman γ line center flux input for *Lyao_rt* code was then estimated using solar Lyman line profile intensity values from Meier (1995) suggesting $Ly_\odot\gamma \approx (1/5.3) \times Ly_\odot\beta$. The assumption that a $Ly_\odot\beta/\gamma$ ratio of 5.3 would hold into solar maximum conditions is not robust.

Lyao_rt was run using the evaporative exospheric extension condition, with (case "H-Param/evap") and without (case "MSIS00/evap") independently specifying the thermospheric hydrogen parameters, $[H]_{peak}$, ϕ and $[H]_{exo}$. A third run (case "H-Param/T-sat") specified additional satellite parameters T_s and n_s. Refer to Table 5. For the H-Param/evap model run, thermospheric dayside H parameters were adopted from Waldrop and Paxton (2013), where we adjusted (only) the $[H]_{exo}$ parameter for the AM and PM density asymmetry based on results from Bishop et al. (2001, 2004). Best fit ϕ values determined by Waldrop and Paxton (2013) are an order of magnitude different between solar maximum ($\sim 10^7$ $cm^{-2}\ s^{-1}$) and minimum ($\sim 10^8$ $cm^{-2}\ s^{-1}$); we have adopted these values for both AM and PM solar conditions for illustrative purposes. The parameterized $[H]_{peak}$ value was held constant (1.5×10^8 cm^{-3}).

The H-Param/T-sat model run uses solar cycle-dependent satellite parameters (T_s and n_s) found by Bishop (1991). Note, T_s inputs were modified in proportion to the NRLMSIS-00 determined variation between AM

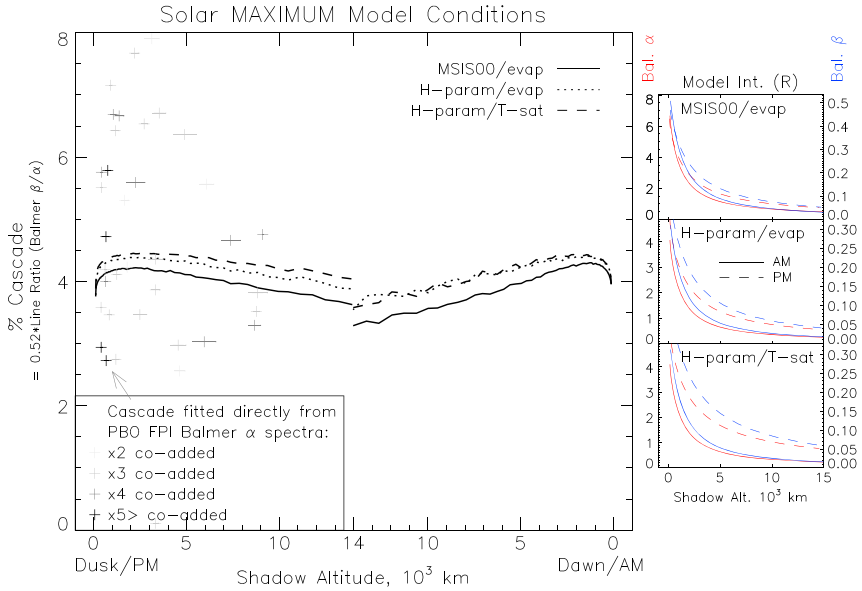

Figure 7. AM and PM solar *maximum* modeled line ratio (expressed as cascade) versus shadow altitude, using three different thermosphere and exosphere model parameterizations (refer to text and Table 5). All three modeled line ratios have nearly equivalent, steeply rising low shadow altitude peak location and magnitudes, followed by broad *negative* curvature toward deeper shadow altitudes. A similar behavior is mildly apparent in the overplotted *darker* crosses for cascade contributions as determined from coadded fits to high-resolution Balmer α line profiles. In the right inset plots, for each modeled Balmer β/α line ratio, the model intensities (R) are plotted where blue (red) traces are for Balmer β (Balmer α) with respect to the right (left) scaled axis.

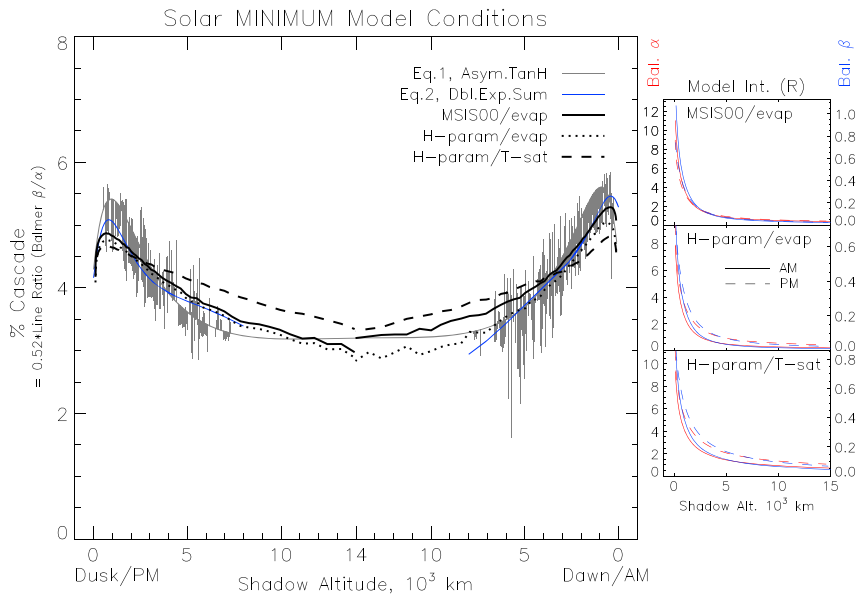

Figure 8. AM and PM solar *minimum* modeled line ratio (expressed as cascade) versus shadow altitude, using different thermosphere and exosphere model parameterizations (refer to text and Table 5). All three modeled line ratios have nearly equivalent, steeply rising low shadow altitude peak location and magnitudes, followed by broad *positive* curvature toward deeper shadow altitudes. A similar behavior is seen in the overplotted gray and blue cascade curves determined from WHAM observations (refer to Figure 5). For right inset plots, refer to Figure 7 caption.

and PM exobase T_c; n_s was held constant. H-Param/evap thermospheric H parameters were adopted in the H-Param/T-sat model runs so that the additionally parameterized satellite population's effect on the Balmer β/α line ratio was distinguishable.

All three forward model generated Balmer β/α line ratios are plotted for solar maximum and minimum conditions in Figures 7 and 8, respectively. The modeled line ratios were obtained by numeric division of the modeled Balmer α and Balmer β intensities (inset plotted on the right of both figures). For the solar maximum run (Figure 7), we overplotted the line ratio equivalent cascade data points, as determined directly from the coadded high-resolution Balmer α spectra. For the solar minimum run (Figure 8), we overplotted the line ratios obtained from WHAM observations of Balmer β and Balmer α, fit by equations (1) (dark gray) and (2) (blue), previously plotted in Figure 5. In both Figures 7 and 8 the solid thick line is for case MSIS00/evap, the dotted line is for case H-Param/evap, and the dashed line is for adding two free satellite parameters to the thermospheric H parameterization (H-param/T-sat).

Comparing Figures 7 and 8, the model line ratio peak position and curvature changes noticeably between the selected solar and geophysical conditions for all three cases. At solar maximum, all three model line ratios indicate a broad peak near a shadow altitude of 2,000 (1,000) km on the PM (AM) side, with a slightly negative curvature toward deep shadow altitudes. The cascade data points (crosses) in Figure 7 suggest general agreement, but there is a large degree of scatter. The model line ratio peak shifts to lower shadow altitudes for solar minimum conditions (Figure 8), more pronounced on the AM side. This consistent variation of line ratio peak magnitude and shadow altitude location (between AM and PM, and also between solar minimum and maximum) appears to be commensurate with exobase temperature variation. Further, the line ratio peak is notably sharper with positive curvature toward deeper shadow altitudes at solar minimum conditions. The overplotted WHAM line ratio observations (equations (1) and (2) in Figure 8) clearly support this model line ratio trend, on both AM and PM sides.

5. Discussion

Having shown that *Lyao_rt* input parameters used in earlier studies generally support the observed Balmer line ratio trend, we now investigate the line ratio for its potential to further constrain forward model retrieved hydrogen parameters. We also review the Balmer line ratio as a constraint for solar Lyman γ-induced cascade in high-resolution Balmer α line profile measurements. Finally, we discuss sources of uncertainty with recommendations to improve future studies.

5.1. Forward Modeling Constraints From Observed Line Ratios

Here we conduct a short sensitivity study (Figure 9), taking systematic steps through a series of thermospheric H parameters in the H-Param/evap AM model case (Table 5), for both solar minimum and maximum conditions. In each panel of Figure 9 only the title parameter is stepped (at the values listed to the right), while the other two parameters are held fixed at the boldface values listed in the other two panels of the same column. Note, for the illustrative purposes of this coarse-grid sensitivity study, interaction between the fixed parameters is ignored. The solar minimum H parameters adopted from Waldrop and Paxton (2013) (shown in Figure 9 as bold line traces at $[H]_{exo} = 2\times10^5$ cm^{-3}, $\phi = 7\times10^8$ cm^{-2} s^{-1}, and $[H]_{peak} = 1.5\times10^8$ cm^{-3}) are consistent with our solar minimum observations in Figure 8 (i.e., where the dotted curve closely matches the blue and the gray curves).

Two general conclusions are drawn from the sensitivity study depicted in Figure 9: (1) the magnitude of the low shadow altitude line ratio peak *increases* with increasing $[H]_{exo}$, while (2) the entire line ratio as a function of shadow altitude *decreases* with increasing ϕ. Both (1) and (2) appear to hold for solar minimum and maximum conditions. Further, the shadow altitude where the line ratio peaks appears to be inversely proportional to $[H]_{exo}$.

The model line ratio sensitivity to ϕ suggests that latitudinal and geophysical variations in ϕ may be detectable in ground-based Balmer β/α line ratio observations of sufficient sensitivity. Referring to the ϕ plots in Figure 9, the difference between top and bottom line ratio curves is about ~1% in cascade magnitude, going from an average/low ϕ to a high (e.g., polar cap) value, respectively. As noted at the end of section 3.4 (Figure 6), WHAM appears sensitive enough to detect average variations in the line ratio (i.e., cascade) magnitude to within ~1%. However, caution is warranted in interpretation as this sensitivity study only employed evaporative (Jean's)

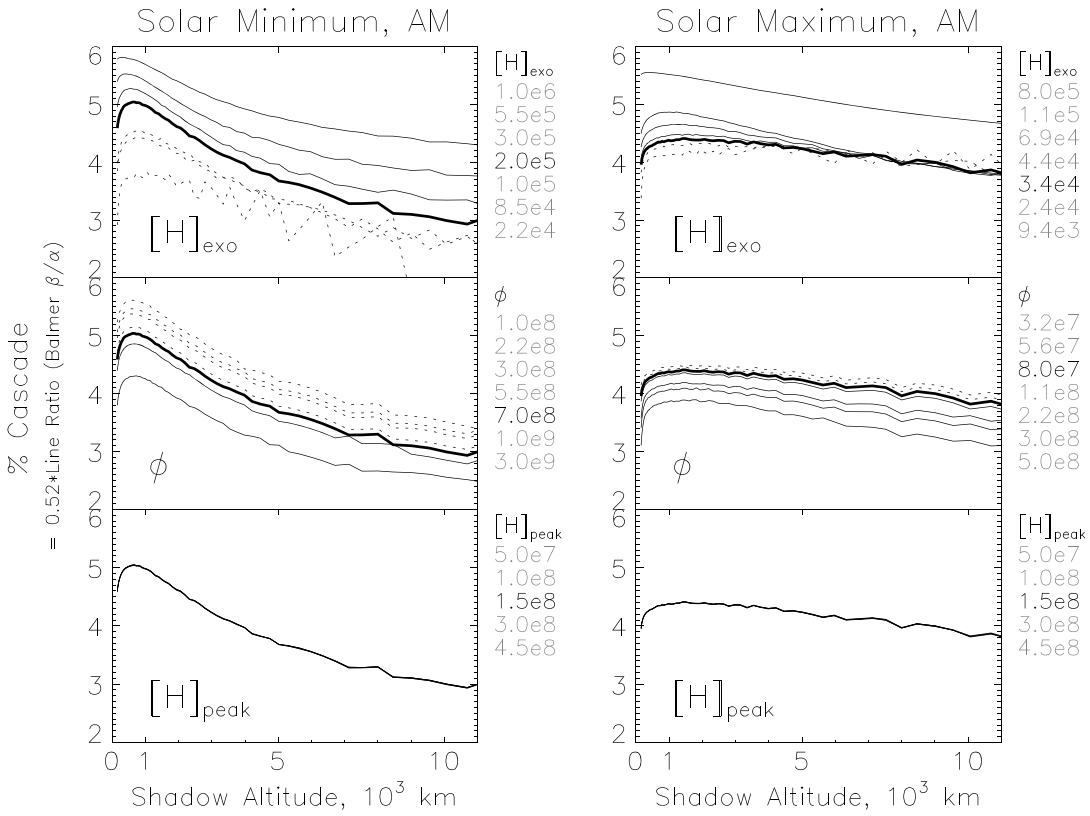

Figure 9. *Lyao_rt* sensitivity case studies of (top) $[H]_{exo}$, (middle) flux ϕ, and (bottom) $[H]_{peak}$, for (right) solar maximum and (left) solar minimum dawnside Balmer β/α line ratios (computed for % cascade at Balmer α using evaporative exosphere conditions). Under each solar condition, the bold trace (and black number to the right) of each respective case study represents the fixed parameter value used for the other two (dashed traces are for *lower* values). Note, line ratio magnitudes are *inversely* proportional to ϕ, insensitive to $[H]_{peak}$, and proportional to $[H]_{exo}$.

escape conditions, and not polar wind or charge exchange escape conditions (Gardner & Schunk, 2004; Johnson et al., 2008; Thomas & Vidal-Madjar, 1978; Yung et al., 1989).

We further investigated the dependence of the shadow altitude location of the Balmer line ratio peak on all three thermospheric H diffusive flow parameters for solar minimum ($F_{10.7}$ = 70.7) and geophysically quiet (AP = 8.4) conditions, using *Lyao_rt*'s evaporative exosphere extension. For both AM and PM cases, 2,280 line ratios were generated using 20 approximately evenly separated values of $[H]_{exo}$ (ranged from 5×10^4 to 1×10^6 cm^{-3}), 19 values of ϕ (ranged between 7×10^7 and 3×10^9 cm^{-2} s^{-1}), and 3 values of $[H]_{peak}$ (1, 1.5, and 3×10^8 cm^{-3}); parameter ranges were selected from previous forward model studies (Bishop et al., 2001; Nossal et al., 2012; Waldrop & Paxton, 2013) and represent reasonable parameter bounds for quiet conditions.

Referring to Figure 10 (top row), the Balmer line ratio's peak shadow altitude location was found to have a strong linear dependence on the natural log of $[H]_{exo}$, with all modeled ϕ and $[H]_{peak}$ values (colored lines and weights, respectively). The following linear fit was obtained for the AM model runs (exobase temperature of 654 K):

$$y = 3039 - 198 \times \ln([H]_{exo}) \quad (3)$$

And similarly, the PM model runs (exobase temperature of 788 K):

$$y = 4254 - 290 \times \ln([H]_{exo}) \quad (4)$$

where y is the observed shadow altitude (km) of the line ratio peak, and $[H]_{exo}$ is in units of cm^{-3}. The slopes of equations (3) and 4 appear to depend on the exobase temperature, T_c.

Referring to Figure 10 (bottom row), the Balmer line ratio's *peak location* was found to be nearly independent of ϕ (and similarly for $[H]_{peak}$, not shown). Note, for each modeled $[H]_{exo}$ value (colored line) we have computed the peak shadow altitude relative difference with respect to the first data point in each model run and then fit

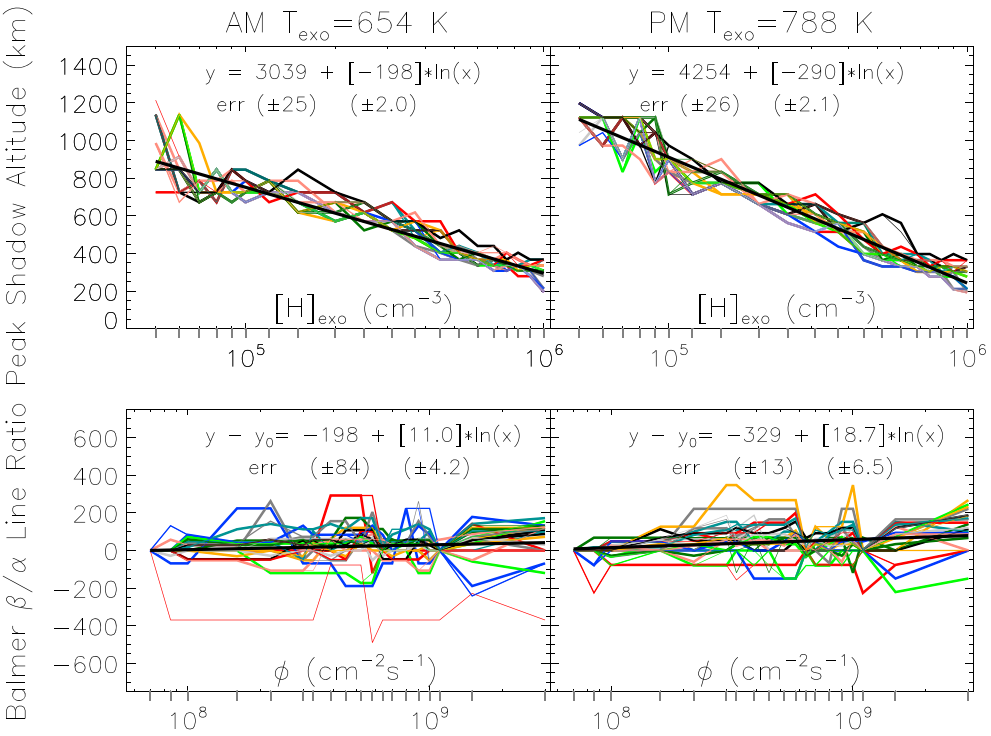

Figure 10. For quiet conditions at (left column) 5 a.m. and (right column) 7 p.m. (right), (top row) absolute shadow altitude location of the Balmer line ratio peak, computed for 20 different (gray tick marked) exobase H densities, using *Lyao_rt*'s evaporative exosphere and H diffusive flow parameterization. (bottom row) Normalized shadow altitude location of Balmer line ratio peak, computed for 19 different H flux values. In the top (bottom) row, different color lines are for varying ϕ ($[H]_{exo}$). Different line weights are for varying $[H]_{peak}$ in both rows (refer to text). Linear fit equations (thick black trace) to the log scale values, and associated coefficient uncertainties printed (beneath), demonstrate the Balmer line ratio peak's shadow altitude location strongly depends on $[H]_{exo}$, for all ϕ.

all runs simultaneously. The slight slope (Figure 10, bottom row) is largely influenced by the extremely high ϕ values ($>10^9$ cm^{-2} s^{-1}), and the random fluctuations are a consequence of model resolution.

The WHAM solar minimum intensity variations fit by equation (1) in Figure 8 indicate line ratio peaks on both the AM and PM sides at a shadow altitude of 900 km—this is due to the symmetry of equation (1). Using the evaporative model H exobase density relationships described by equations (3) and 4, these shadow altitude peak locations correspond to AM and PM exobase H densities of 4.9×10^4 and 1.1×10^5 cm^{-3}, respectively. These values are not in agreement with observations or models, indicating equation (1) is invalid for line ratio peak analysis.

Equation (2) fits to WHAM data give line ratio shadow altitude peaks on the AM and PM sides at 416 and 808 km, respectively. By equations (3) and 4, these shadow altitude peaks correspond to AM and PM exobase H densities of 5.7×10^5 and 1.5×10^5 cm^{-3}, respectively. This PM exobase H density value is consistent with that (1.6×10^5 cm^{-3}) reported by Waldrop and Paxton (2013) from forward model fits to GUVI Lyman α data taken during the same solar minimum period (2008). Further, the increase in AM density by a factor of ~3.8 (relative to PM) found here agrees well with the findings of Bishop et al. (2001) of a factor of ~3 increase in exobase H density between AM and PM (5.7 and 1.9×10^5 cm^{-3}, respectively) retrieved from forward model fits to Balmer α data, for similar solar minimum (1,988) and geophysical conditions.

Recall that the line ratio variation with shadow altitude arises because Balmer α and Balmer β intensities fall off exponentially at different rates due to scattering (opacity) differences between Lyman γ and Lyman β through the same hydrogen atmosphere. The low shadow altitude line ratio *peak*, where the line ratio slope is zero, must occur *at* a shadow altitude where the ratio of the *rate of change* of intensity (of Balmer β to Balmer α) equals the magnitude of the Balmer β/α line ratio itself. In principle, this suggests an empirical relationship could be determined relating the peak line ratio (or cascade) directly to column density.

The reason there is a line ratio peak *at all* is because Balmer β intensities are initially decreasing less rapidly than Balmer α with (low) shadow altitude, due to the Lyman γ screening altitude being higher than that of Lyman β (and well above the mesospheric peak H region, near 80 km). Noting Table 1 values, as one moves from solar minimum to maximum, the Balmer line ratio peak shadow altitude location could be anticipated to move to higher shadow altitudes, precisely because the Lyman γ screening altitude also advances to higher altitudes (although changes in the density distribution itself would also have to be considered). As one moves through higher altitudes, multiple scattering contributions to Balmer α slow its decrease relative to Balmer β and the line ratio decreases.

Referring to Figure 8, the WHAM-observed line ratio curvature obtained using equation (2) (blue curve), from 2,000 to 7,000 km agrees well with the H-Param/evap model run (the dotted curve). However, the still-higher observed line ratio peak magnitude, and lower tail, particularly on the AM side, suggests WHAM line ratio observations may be hinting at some combination of *higher* H flux, ϕ, *and/or higher-still* exobase densities, $[H]_{exo}$. Caution is warranted here since the satellite population parameters' effect on the Balmer line ratio has not been examined in detail. This is beyond the scope of this manuscript.

Lyao_rt satellite H parameterization (accounting for temperature dependent charge exchange population repartitioning) can substantially increase exospheric column densities. The right-side inset intensities in Figures 7 and 8, across model runs and between AM and PM conditions (dashed versus solid), illustrates the sensitivity of the column emission (and thus the exospheric [H(z)] profile) to changes in the exobase and satellite atom temperatures ΔT_c and ΔT_s, respectively (refer to Table 5). Referring to the top two inset graphs in Figure 8, the MSIS00/evap model most accurately reproduces observed solar minimum intensity magnitudes at the lowest shadow altitudes (12–14 R for Balmer α), but only with the inclusion that satellite parameters do the intensity magnitudes at deeper shadow altitudes begin to agree with observations ($\sim$1 R for Balmer α). Both evaporative extensions appear to do a better job at reproducing the observed line ratio curvature, but both fail to reproduce the individual intensity variations at deeper shadow altitudes. The comparatively large differences in forward modeled *intensity* magnitudes between separate model parameterizations, compared with the general agreement in the *line ratio* magnitude illustrates our assertion that the *observed* line ratio can give forward model results of [H(z)] that are nearly independent of absolute calibration.

5.2. Balmer α Line Profile Constraints From Observed Line Ratios

Figure 7 suggests the fits to the high-resolution Balmer α spectra may be capturing more than just the signature of cascade (i.e., the crosses are generally higher than the model line ratio curves), although it is also clear that there is significant scatter in the coadded data. The darker crosses, however, being indicative of more confidence in cascade determination based on the coaddition of a higher number of spectra, do corroborate the model line ratio's general behavior, i.e., a sharp rise at low shadow altitude, followed by a generally broad fall off to higher shadow altitudes.

Assuming for the moment that any of the solar maximum model line ratios in Figure 7 were actual simultaneous WHAM-observed line ratios, the *expected* cascade contribution to Balmer α due to solar Lyman γ could be determined, and the fine structure cascade fits to the Balmer α line profiles could be constrained. If this were the case, the difference between the dark crosses in Figure 7, and the line ratio curves *below*, might indicate the presence of additional excitation from photoelectron impact or symmetric charge exchange at low shadow altitudes. Note, the expected contribution from exospheric dynamic signatures to the Balmer α profile, in excess of solar Lyman γ induced cascade, is thought to be small at the shadow altitudes investigated here (Bishop & Chamberlain, 1987; Yelle & Roesler, 1985), whereas symmetric charge exchange interactions could be more consequential due to increased H densities at these low shadow altitudes.

The key utility here is that relatively *low-resolution* WHAM measurements of the Balmer β/α line ratio variation with shadow altitude allow for cascade corrections to *high-resolution* Balmer α observations. So long as the average geophysical conditions are similar between sets of observations, the cascade variations as determined here by WHAM could be applied to high-resolution observations that are not necessarily coincident (albeit with greater uncertainty).

5.3. Current Limitations

A detailed fine-grid forward model parameter study is needed to further explore the full extent of the exosphere's (e.g., satellite atoms) effect on the Balmer line ratio. A few points regarding possible limitations should be mentioned when approaching such a task, as well as when interpreting our current model results

and observational data. Below we discuss data variance possibilities, potential model biases, and errors in intensity fitting.

5.3.1. Data Variances

The general magnitude of agreement between our modeled and observed Balmer line ratios indicates our estimated *Lyao_rt* input ratio of solar Lyman $\beta/\gamma \approx 5.3$ was accurate for solar minimum conditions. However, we did not examine adjustments in the solar Lyman line center ratio because it simply scales the modeled Balmer line ratio. Note, at low shadow altitudes, where single scattering dominates the observed emission, rapid variations in the Balmer line ratio peak magnitudes may correlate more strongly with non-commensurate solar Lyman γ and Lyman β variation than [H(z)] variation (Meier, 1991).

Further, Table 4 lists several late 2000 dates with relatively high *daily averaged Dst*, indicating even *higher* peak *Dst* values corresponding to weak substorms. Using TWINS satellite Lyman α data, Zoenchen et al. (2017) showed a nonnegligible range of 9–23% neutral H column density increases during geomagnetic storms of similar *Dst* values. Geomagnetic storms are associated with enhanced upper thermospheric charge exchange (Daglis et al., 1999), and the associated increase in H satellite population would affect the Balmer line ratio curvature. A temporally correlative comparison of Balmer line ratio data variances with solar activity and *Dst*, however, is beyond the scope of this current work.

5.3.2. Potential Model Biases

In Figure 8 the forward modeled line ratios do *not* meet at the midnight shadow altitude, 14,000 km. This discontinuity is a consequence of our model runs being computed for *only* two local times, 7 p.m. and 5 a.m. Future forward modeling work, with more extensive WHAM line ratio observations, will generate source function arrays sampling a range of local times and/or will incorporate midnight averaging to blend AM and PM model distributions.

Similarly, our current *Lyao_rt* inputs do not attempt to fully account for the AM/PM asymmetry as the code was run for only two local times using a spherically symmetric atmosphere and uniform exobase temperature and density conditions. Also, the version of *Lyao_rt* used here employs a discrete exobase transition. Results by Qin and Waldrop (2016) indicate that the use of a smooth exobase transition region led to better agreement with GUVI observations. Also note that *Lyao_rt*'s use of tabulated temperature-independent cross sections for thermospheric absorption calculations may impact model scattering intensities, particularly at low shadow altitudes near the line ratio peak position.

The modeled line ratio peak shadow altitude was found sensitive to the geophysical model input conditions, shifting from ~500 to 2,000 km in our initial exploratory modeling study. As discussed in section 2.1, the shadow altitude calculation itself may affect the precise location of the observed line ratio peak in shadow altitude space. For example, not differentiating for the solar cycle and geophysical variation on the vertical optical depth used to define shadow altitude may impose a small model bias.

For our present observations, none of these biases are anticipated to be of any significant consequence due to the length of our exposure times and the calibration uncertainty in the data. Future observations may make these distinctions in defining shadow altitude more significant when using the line ratio as a constraint to retrieving forward model parameters.

5.3.3. Intensity Fitting Errors

Regarding fitting of the intensity variations in Figure 4, both equations (1) and (2) indicate a line ratio peak at low shadow altitudes. While equation (1) can extrapolate to midnight intensities and capture the AM *intensity* asymmetry, it cannot, by current design, capture the AM/PM peak shadow altitude *location* asymmetry. Equation (2) captures both the AM/PM asymmetry in peak location and intensity, but differing midnight intensity minima are obtained—a result not consistent with observations.

Here equation (1) aided in bootstrapping parameter constraints (the intensity minima) for the more physically motivated equation (2). Equation (1) is flexible enough to fit log or nonlog intensity variations with periodic, symmetric pole-like behavior about any unfolding shadow altitude to span AM and PM data. Note, in lieu of unfolding about a shadow altitude for which there is no data spanning AM to PM, the *absolute magnitude* of equation (1) could be used to fit discontinuous midnight intensity variations.

The coefficient errors listed in Table 3 for equation (1) are large for fit parameters *A* and *C*—the amplitude and sharpness, which give a delta-function-like punctuation of the distorting second degree polynomial in equation (1) at the complex pole frequency (parameter B). This is a consequence of data scatter, and motivated

our choice to fit equation (1) to the log(intensity) data and equation (2) to the intensity data, helping confirm the observed Balmer line ratio peak. Thus, we do not compare χ^2 values here, as these are two different fitting functions to two different data variations.

6. Conclusion

The two largest physical variables affecting the observed Balmer β/α line ratio as a function of shadow altitude, and thus the magnitude of the cascade contribution to Balmer α, are (1) the ratio of the solar Lyman γ/β line center fluxes and (2) the geocoronal H density distribution itself, [H(z)]. To precisely untangle between effects from [H(z)] and from solar Lyman ratio variations on the present observations, a full forward modeling study would be needed.

Toward that end, the magnitude of the expected cascade contribution to the Balmer α line profile derived from WHAM line ratio observations at low shadow altitudes is shown to be in agreement with historical measurements, ~5% (see, e.g., Meier, 1995; Mierkiewicz et al., 2006). The observed Balmer line ratio scaling and fit residuals suggest that WHAM can detect an average cascade variation with shadow altitude to ~1% uncertainty (in cascade). The line ratio measurements made by WHAM during solar minimum show a clear low shadow altitude peak, and positive curvature trend, with shadow altitude (Figure 8); this trend was corroborated by forward modeling. A notable solar cycle influence on the Balmer line ratio curvature and peak location with shadow altitude was also suggested by forward modeling (Figure 9). Reanalysis of the cascade contribution obtained directly from profile fits to coadded high-resolution solar maximum PBO Balmer α spectra roughly corroborates the solar cycle's influence on the modeled line ratio, indicating a possible negative curvature trend with shadow altitude (Figure 7). Further, the observed Balmer β/α line ratio peak and curvature are likely robust forward model constraints for obtaining the underlying [H(z)] distribution, without direct knowledge of the absolute solar Lyman line center fluxes or absolute instrumental intensity calibration (only their ratios are needed).

For evaporative (Jean's escape) exospheric conditions, the Balmer line ratio peak location in shadow altitude depends only on the natural log of the exobase density, $[H]_{exo}$ (and thus also on T_c). Example AM and PM case relationships were shown for solar minimum, geophysically quiet conditions in equations (3) and 4, where we found similar solar minimum AM and PM exobase H densities as reported by Bishop et al. (2001). Increases in $[H]_{exo}$ lead to increases in the line ratio peak magnitude. However, the line ratio magnitude decreases with increasing H flux, ϕ (which also appears to not influence this shadow altitude peak location). This suggests solar cycle/T_c-dependent relationships may exist constraining ϕ and $[H]_{exo}$ parameters due to their *opposite* effects on line ratio peak magnitude and width.

In summary, we have shown the first observational evidence for a variation of cascade emission with shadow altitude, as observed by WHAM Balmer β/α line ratios. We also show that independent fitting of high-resolution PBO FPI Balmer α spectral line profiles, with a full fine structure model to determine the cascade contribution to observed Balmer α intensity, corroborates the cascade variation calculated by WHAM. Taken together, a key utility of this work is that relatively low-resolution WHAM measurements of the Balmer β/α line ratio variation with shadow altitude allow for cascade corrections to, or constraints for, high-resolution Balmer α observations.

In addition to demonstrating firm agreement among diverse data sets, we have also demonstrated that the empirical Balmer β/α line ratio trend (i.e., the shape of the cascade variation with shadow altitude) serves as a tight constraint in the forward model retrieval of exospheric H parameters from ground-based Balmer series observations. In fact, exploratory forward modeling of the line ratio, using parameters adopted from earlier forward modeling studies, was shown to be consistent with our observed Balmer line ratio (i.e., cascade) trends.

Acknowledgments
The authors would like to thank the referees for their constructive comments improving the manuscript. Special thanks are due to D. Bruning for invaluable help dissecting Lyao_rt legacy Fortran issues and to S. Solomon for helpful suggestions and the GLOW model subset routines. We also thank C. Woodward and J. Percival for their continued assistance with VF spectral fitting routine and shadow altitude computation routine, respectively. This work has been funded by the National Science Foundation (NSF) through awards AGS 1347687 and AGS 1352311; WHAM is supported by NSF award AST 1108911. Data sets for this paper have been processed using IDL (v8.2), supported with Astronomy Library plug-ins. All IDL source codes and data sets are freely available from the authors upon request.

References

Anderson, D. E. Jr., & Hord, C. W. (1977). Multidimensional radiative transfer: Applications to planetary coronae. *Planetary and Space Science*, *25*, 563–571.

Anderson, D. E., Jr., Meier, R. R., Hodges, R. R., & Tinsley, B. A. (1987). Hydrogen Balmer alpha intensity distributions and line profiles from multiple scattering theory using realistic geocoronal models. *Journal of Geophysical Research*, *92*, 7619–7642. https://doi.org/10.1029/JA092iA07p07619

Bailey, J., & Gruntman, M. (2011). Experimental study of exospheric hydrogen atom distributions by Lyman-alpha detectors on the TWINS mission. *Journal of Geophysical Research*, *116*, A09302. https://doi.org/10.1029/2011JA016531

Bishop, J. (1991). Analytic exosphere models for geocoronal applications. *Planetary and Space Science*, *39*, 885–893.
Bishop, J. (1999). Transport of resonant atomic hydrogen emissions in the thermosphere and geocorona: Model description and applications. *Journal of Quantitative Spectroscopy and Radiative Transfer*, *61*(4), 473–491.
Bishop, J. (2001). Thermospheric atomic hydrogen densities and fluxes from dayside Lyman α measurements. *Journal of Atmospheric and Solar-Terrestrial Physics*, *63*, 331–340.
Bishop, J., & Chamberlain, J. W. (1987). Geocoronal structure: 3. Optically thin, Doppler-broadened line profiles. *Journal of Geophysical Research*, *92*(A11), 12,389–12,397. https://doi.org/10.1029/JA092iA11p12389
Bishop, J., Harlander, J. M., Nossal, S. M., & Roesler, F. L. (2001). Analysis of Balmer α intensity measurements near solar minimum. *Journal of Atmospheric and Solar-Terrestrial Physics*, *63*, 341–353.
Bishop, J., Mierkiewicz, E. J., Roesler, F. L., Gomez, J. F., & Morales, C. (2004). Data-model comparison search analysis of coincident PBO Balmer α, EURD Lyman β geocoronal measurements from March 2000. *Journal of Geophysical Research*, *109*, A05307. https://doi.org/10.1029/2003JA010165
Chamberlain, J. W., & Hunten, D. M. (1987). *Theory of Planetary Atmospheres: An Introduction to Their Physics and Chemistry* (2nd ed., pp. 330–415). Orlando, FL: Academic Press.
Coakley, M. M., Roesler, F. L., Reynolds, R. J., & Nossal, S. (1996). Fabry-Perot/CCD annular summing spectroscopy: Study and implementation for aeronomy applications. *Applied Optics*, *35*, 6479.
Daglis, I. A., Thorne, R. M., Baumjohann, W., & Orsini, S. (1999). The terrestrial ring current: Origin, formation, and decay. *Reviews of Geophysics*, *37*, 407–438.
Fahr, H. J., & Shizgal, B. (1983). Modern exospheric theories and their observational relevance. *Reviews of Geophysics and Space Physics*, *21*(1), 75–124.
Fennelly, J. A., & Torr, D. G. (1992). Photoionization and photoabsorption cross sections of O, N_2, O_2, and N for aeronomic calculations. *Atomic Data and Nuclear Data Tables*, *51*, 321.
Gardner, D. D., Mierkiewicz, E. J., Roesler, F. L., Harlander, J. M., Jaehnig, K. P., Nossal, S. M., & Haffner, L. M. (2017). First performance results of a new field-widened spatial heterodyne spectrometer for geocoronal Hα research. *Journal of Geophysical Research: Space Physics*, *121*, 1373–1385. https://doi.org/10.1002/2016JA022625
Gardner, L. C., & Schunk, R. W. (2004). Neutral polar wind. *Journal of Geophysical Research*, *109*, A05301. https://doi.org/10.1029/2003JA010291
Haffner, L. M., Reynolds, R. J., Tufte, S. L., Madsen, G. J., Jaehnig, K. P., & Percival, J. W. (2003). The Wisconsin H-alpha mapper northern sky survey. *Astrophysical Journal Supplement Series*, *149*(2), 405–422.
Hausen, N. R., Reynolds, R. J., & Haffner, L. M. (2002). Interstellar Hα line profiles towards HD 93521 and the Lockman Window. *Astrophysical Journal*, *565*, 1060–1068.
He, X., Kerr, R. B., Bishop, J., & Tepley, C. A. (1993). Determining exospheric hydrogen density by reconciliation of Hα measurements with radiative transfer theory. *Journal of Geophysical Research*, *98*, 21,611–21,628.
Hedin, A. E. (1991). Extension of the MSIS thermospheric model into the middle and lower atmosphere. *Journal of Geophysical Research*, *96*, 1159–1172.
Hong, S. S., Kwon, S. M., Park, Y. S., & Park, C. (1998). Transfer of diffuse astronomical light and airglow in scattering Earth atmosphere. *Earth Planets Space*, *50*, 487–491.
Hunten, D. M., & Donahue, T. M. (1976). Hydrogen loss from the terrestrial planets. *Annual Review of Earth and Planetary Sciences*, *4*, 265–292.
Johnson, R. E., Combi, M. R., Fox, J. L., Ip, W. H., Leblanc, F., McGrath, M. A., … Waite, J. H. (2008). Exospheres and atmospheric escape. *Space Science Reviews*, *139*, 355–397.
Krall, J., & Huba, J. D. (2016). The plasmasphere electron content paradox. *Journal of Geophysical Research: Space Physics*, *121*, 8924–8935. https://doi.org/10.1002/2016JA023008
Krall, J., Huba, J. D., Jordanova, V. K., Denton, R. E., Carranza, T., & Moldwin, M. B. (2016). Measurements and modeling of the refilling plasmasphere during 2001. *Journal of Geophysical Research: Space Physics*, *121*, 2226–2248. https://doi.org/10.1002/2015JA022126
Krall, J., Emmert, J. T., Sassi, F., McDonald, S. E., & Huba, J. D. (2016). Day-to-day variability in the thermosphere and its impact on plasmasphere refilling. *Journal of Geophysical Research: Space Physics*, *121*, 6889–6900. https://doi.org/10.1002/2015JA022328
Kerr, R. B., Garcia, R., He, X., Noto, J., Lancaster, R. S., Tepley, C. A., … McCormack, B. (2001). Periodic variations of geocoronal Balmer-alpha brightness due to solar-driven exospheric abundance variations. *Journal of Geophysical Research*, *106*(A12), 28,797–28,817. https://doi.org/10.1029/1999JA900186
Leinert, C., Bowyer, S., Haikala, L. K., Hanner, M. S., Hauser, M. G., Levasseur-Regourd, A. C., … Witt, A. N. (1998). The 1997 reference of diffuse night sky brightness. *Astronomy and Astrophysics Supplement Series*, *127*, 1–99.
Madsen, G. J., & Reynolds, R. J. (2005). An investigation of diffuse interstellar gas toward a large, low-extinction window into the inner galaxy. *Astrophysics Journal*, *630*, 925–944.
Meier, R. R. (1991). Ultraviolet spectroscopy and remote sensing of the upper atmosphere. *Space Science Reviews*, *58*, 1–185.
Meier, R. R. (1995). Solar Lyman series line profiles and atomic hydrogen excitation rates. *Astrophysical Journal*, *452*, 462–471, with Erratum (1996). *Astrophysical Journal*, *468*, 455.
Meriwether, J. W., Atreya, S. K., Donahue, T. M., & Burnside, R. G. (1980). Measurements of the spectral profile of Balmer alpha emission from the hydrogen geocorona. *Geophysics Research Letter*, *452*(11), 967–970.
Mierkiewicz, E. J. (2002). Fabry–Perot observations of the hydrogen geocorona (PhD Thesis), Madison: University of Wisconsin.
Mierkiewicz, E. J., Roesler, F. L., Bishop, J., & Nossal, S. M. (1999). A systematic program for ground-based Fabry–Perot observations of the neutral hydrogen exosphere. *Proceedings of SPIE*, *3756*, 323–336. https://doi.org/10.1117/12.366386
Mierkiewicz, E. J., Roesler, F. L., & Nossal, S. M. (2012). Observed seasonal variations in exospheric effective temperatures. *Journal of Geophysical Research*, *117*, A06313. https://doi.org/10.1029/2011JA017123
Mierkiewicz, E. J., Roesler, F. L., Nossal, S. M., & Reynolds, R. J. (2006). Geocoronal hydrogen studies using Fabry–Perot interferometers, Part 1: Instrumentation, observations, and analysis. *Journal of Atmospheric and Solar-Terrestrial Physics*, *68*, 1520–1552.
Nossal, S. M., Mierkiewicz, E. J., & Roesler, F. L. (2012). Observed and modeled solar cycle variation in geocoronal hydrogen using NRLMSISE-00 thermosphere conditions and the Bishop analytic exosphere model. *Journal of Geophysical Research*, *117*, A03311. https://doi.org/10.1029/2011JA017074
Nossal, S. M., Mierkiewicz, E. J., Roesler, F. L., Haffner, L. M., Reynolds, R. J., & Woodward, R. C. (2008). Geocoronal hydrogen observations spanning three solar minima. *Journal of Geophysical Research*, *113*, A11307. https://doi.org/10.1029/2008JA013380

Nossal, S. M., Roesler, F. L., & Coakley, M. M. (1998). Cascade excitation in geocoronal hydrogen Balmer-α line. *Journal of Geophysical Research*, *103*(A1), 381–390.

Nossal, S. M., Roesler, F. L., Reynolds, R. J., Haffner, L. M., Tufte, S., Bishop, J., … Mierkiewicz, E. J. (2001). Geocoronal Balmer α intensity measurements using the WHAM Fabry–Perot facility. *Journal of Geophysical Research*, *106*, 5605–5616.

Picone, J. M., Hedin, A. E., Drob, D. P., & Aikin, A. C. (2002). NRLMSISE-00 empirical model of the atmosphere: Statistical comparisons and scientific issues. *Journal of Geophysical Research*, *107*, 1468. https://doi.org/10.1029/2002JA009430

Pierrehumbert, R. T. (2010). *Principles of Planetary Climate* (1st ed., pp. 534–587). Cambridge, UK: Cambridge University Press.

Qin, J., & Waldrop, L. (2016). Non-thermal hydrogen atoms in the terrestrial upper thermosphere. *Nature Communications*, *7*, A13655. https://doi.org/10.1038/ncmoms13655

Richards, P. G., Fennelly, J. A., & Torr, D. G. (1994). EUVAC: A solar EUV flux model for aeronomic calculations. *Journal of Geophysical Research*, *99*, 8981–8992.

Roesler, F. L. (1974). Fabry–Perot instruments for astronomy. In M. Carlton (Ed.), *Methods of experimental physics, Part A: Optical and infrared* (Vol. 12, pp. 531). New York: Academic Press.

Roesler, F. L., Mierkiewicz, E. J., & Nossal, S. M. (2014). The geocoronal Hα cascade component determined from geocoronal Hβ intensity measurements. *Journal of Geophysical Research: Space Physics*, *119*, 6642–6647. https://doi.org/10.1002/2014JA020026

Scherb, F. (1981). Hydrogen production rates from ground-based Fabry–Perot observations of comet Kohoutek. *Astrophysical Journal*, *243*, 644–650.

Shih, P., Roesler, F. L., & Scherb, F. (1985). Intensity variations of geocoronal Balmer alpha emission: 1. Observational results. *Journal of Geophysical Research*, *90*, 477–490.

Solomon, S. C. (2017). Global modeling of thermospheric airglow in the far-ultraviolet. *Journal of Geophysical Research: Space Physics*, *122*, 7834–7848. https://doi.org/1002/2017JA024314

Thomas, G. E., & Vidal-Madjar, A. (1978). Latitude variations of exospheric hydrogen and polar wind. *Planetary and Space Science*, *26*, 863–871.

Tinsley, B. A. (1968). Temporal variations in geocoronal Balmer alpha. *Journal of Geophysical Research*, *73*(13), 4139–4149.

Tufte, S. L. (1997). The WHAM spectrometer: Design performance characteristics and first results (PhD Thesis), Madison: University of Wisconsin.

Waldrop, L. S., & Paxton, L. J. (2013). Lyman alpha airglow emission: Implications for atomic hydrogen geocorona variability with solar cycle. *Journal of Geophysical Research: Space Physics*, *118*, 5874–5890. https://doi.org/10.1002/jgra.50496

Warren, H. P., Mariska, J. T., & Wilhelm, K. (1998). High-resolution observations of the solar hydrogen Lyman lines in the quiet Sun with the SUMER instrument on SOHO. *Astrophysical Journal Supplement Series*, *119*, 105–120.

Yelle, R. V., & Roesler, F. L. (1985). Geocoronal Balmer alpha line profiles and implication for the exosphere. *Journal of Geophysical Research*, *90*, 7568–7580.

Yung, Y. L., Wen, J. S., Moses, J. I., Landry, B. M., Allen, M., & Hsu, K. J. (1989). Hydrogen and deuterium loss from the terrestrial atmosphere: A quantitative assessment of nonthermal escape fluxes. *Journal of Geophysical Research*, *94*, 14,971–14,989.

Zoenchen, J. H., Nass, U., Fahr, H. J., & Goldstein, J. (2017). The response of the H geocorona between 3 and 8 R_e to geomagnetic disturbances studied using TWINS stereo Lyman-α data. *Annales Geophysicae*, *35*, 171–179.